



UNIVERSITÀ  
DEGLI STUDI  
FIRENZE

## FLORE

# Repository istituzionale dell'Università degli Studi di Firenze

### **Dimensionless numbers for the assessment of mesh and timestep requirements in CFD simulations of Darrieus wind turbines**

Questa è la Versione finale referata (Post print/Accepted manuscript) della seguente pubblicazione:

*Original Citation:*

Dimensionless numbers for the assessment of mesh and timestep requirements in CFD simulations of Darrieus wind turbines / Balduzzi, Francesco; Bianchini, Alessandro; Ferrara, Giovanni; Ferrari, Lorenzo. - In: ENERGY. - ISSN 0360-5442. - ELETTRONICO. - 97:(2016), pp. 246-261. [10.1016/j.energy.2015.12.111]

*Availability:*

The webpage <https://hdl.handle.net/2158/1019409> of the repository was last updated on 2021-03-30T14:30:13Z

*Published version:*

DOI: 10.1016/j.energy.2015.12.111

*Terms of use:*

Open Access

La pubblicazione è resa disponibile sotto le norme e i termini della licenza di deposito, secondo quanto stabilito dalla Policy per l'accesso aperto dell'Università degli Studi di Firenze (<https://www.sba.unifi.it/upload/policy-oa-2016-1.pdf>)

*Publisher copyright claim:*

La data sopra indicata si riferisce all'ultimo aggiornamento della scheda del Repository FloRe - The above-mentioned date refers to the last update of the record in the Institutional Repository FloRe

(Article begins on next page)

# Dimensionless numbers for the assessment of mesh and timestep requirements in CFD simulations of Darrieus wind turbines

Francesco BALDUZZI<sup>1a</sup>, Alessandro BIANCHINI<sup>1b</sup>, Giovanni FERRARA<sup>1c</sup>, Lorenzo FERRARI<sup>2d\*</sup>

<sup>1)</sup> Department of Industrial Engineering, University of Florence  
Via di Santa Marta 3, 50139, Florence, Italy  
Phone +39 055 275 8773

<sup>2)</sup> CNR-ICCOM, National Research Council of Italy  
Via Madonna del Piano 10, 50019, Sesto Fiorentino, Italy  
\* Phone +39 055 5225 218 - Fax +39 055 5225 203

## Abstract

Computational Fluid Dynamics is thought to provide in the near future an essential contribution to the development of Vertical-Axis Wind Turbines.

The unsteady flow past rotating blades is, however, a challenging application for a numerical simulation and some critical issues have not been settled yet. In particular, if some studies in the literature report detailed analyses on the assessment of the computational model, there is still no adequate convergence on the requirements in terms of spatial and temporal discretizations.

In the present study, a multivariate sensitivity analysis was first carried out on a specific case study at different tip-speed ratios in order to define the optimal mesh and timestep sizes needed for an accurate simulation. Once full insensitivity had been reached, the spatial and temporal requirements needed to properly describe the flow phenomena were related to two dimensionless numbers, one for each domain, which can be used to assess the suitability of the selected settings for each specific simulation.

The simulations revealed that the spatial requirements must be selected in order to ensure an accurate description of velocity gradients in the near-blade region. To this purpose, a Grid-Reduced form of vorticity is proposed as the best indicator for the quality of the mesh refinement.

It is also shown that the temporal requirements are made stricter at low tip-speed ratios by the need of correctly describing the vortices detaching from the blades in the upwind region. To do so, proper thresholds for the Courant Number are highlighted in the study.

**Keywords:** CFD; Darrieus; VAWT; vorticity; Courant Number; mesh sensitivity;

## 1. Introduction

In the last decade, increasing interest among renewable energy sources has been paid to Vertical-Axis Wind Turbines (VAWTs) [1]-[5]. To study these machines, one-dimensional models based on the Blade Element Momentum (BEM) theory have been extensively used in the past, in particular to identify the first design solutions [6]-[10].

Due to the intrinsic limitations of one-dimensional models, however, more recently the attention of the scientific community has been focused on CFD simulations (e.g. [11]-[12]), which are thought to shortly

*a) balduzzi@vega.de.unifi.it*

*b) bianchini@vega.de.unifi.it*

*c) giovanni.ferrara@unifi.it*

*d) lorenzo.ferrari@iccom.cnr.it (corresponding author)*

enable a more in-depth understanding of the aerodynamic behavior of blades rotating around an axis orthogonal to flow direction and of many connected issues, e.g. aero-acoustic noise [13]. The use of higher-order methods to improve the understanding of wind energy phenomena is indeed one of the main challenges for the research [14-15].

Since fully unsteady phenomena need to be captured, a proper numerical setup is needed for an accurate numerical simulation. In particular, the low tip-speed ratios (TSRs) are characterized by a large variation of the incidence angle during each revolution. In these conditions, non-stationary phenomena take place, e.g. the onset of dynamic stall structures and vortex shedding. An accurate prediction of all these flow features is therefore pivotal to correctly predict the machine performance in these functioning conditions. Since high local gradients of the flow quantities are associated to the vortices generation, the computational method and the mesh topology must be properly related to the requirements for resolving the physics of the problem.

While the suitability of the modeling strategy (turbulence, numerical schemes, algorithm, etc.) is not a priori evaluable [16] the choices made in terms of spatial and temporal discretization lead to the generation of numerical errors that can be theoretically evaluated and minimized. As a general reference, the mesh resolution must be defined according to the gradients intensity in order to accurately compute the spatial variation of the flow quantities and to limit the numerical diffusion, especially in the case of CFD approaches using unstructured meshes. The greater are the gradients, the finer must be the mesh. The order of the difference schemes can be preserved and the grid related error may be virtually eliminated. Verification is mandatory to ensure that a CFD code can correctly produce a solution for the mathematical equations used in the conceptual model, although it does not necessarily imply that the computational results actually represent the physical phenomenon.

Some works have been presented in literature [17]-[28] reporting detailed analyses on the assessment of the proper computational model but there is still no adequate comprehension or convergence on the CFD requirements. In the majority of these works, the numerical model is investigated only at a superficial level, with focus only on the sensitivity analyses to the grid refinement, timestep or turbulence model.

The information provided are mostly case dependent and, therefore, of scarce practical use. An example of a higher-level study was proposed by Trivellato [29], aimed at assessing the size of the grid elements at the rotating interface and the angular marching step by exploiting the Courant-Friedrichs-Lewy (CFL) criterion. In particular, it was found that angular timesteps in the order of  $1/15^\circ$  or  $1/30^\circ$  are advisable to minimize numerical errors, due to the effects of the CFL criterion on relevant local properties (such as the torque coefficient as a function of the blade azimuthal position).

In order to achieve a mesh independent solution, Almohammadi [21] pointed out by means of an extensive literature review that, although extensive research has been carried out to obtain reasonable agreement between CFD results and experimental data, no single study exists in the literature that adequately covers a grid independency analysis. To this purpose, Almohammadi suggested the use of advanced methods for the investigation of the mesh independency. In particular, he made use of extrapolation-based error estimators as the General Richardson Extrapolation (GRE) and the Grid Convergence Index (GCI), which are largely recommended for verification studies in computational fluid dynamics [30]-[33].

In previous works ([11] and [34]), the authors showed the necessity of defining very heavy meshes, particularly due to the high number of nodes needed on the airfoils' surface. Moreover, the need of both an increase of the mesh resolution and a reduction of the angular timestep were noticed in case of low revolution speeds of the rotor. These operating conditions are more critical due to the wider range of incidence angles that enhances the stall phenomenon.

In the present study, the results of a deep and systematic sensitivity analysis were analyzed in order to identify the correlation between the requirements in terms of spatial and temporal resolution and the physics to be solved. In the first part of the activity, the CFD requirements throughout the whole operating range of the machine were identified. This goal was achieved by analyzing a large set of operating points which were simulated considering different meshes, angular timesteps and rotating speeds. In the second part, the authors identified the relationship between the physical properties of the flow and the assessed discretization properties of the numerical model by making use of newly proposed dimensionless numbers. The main aim of the study was then to define some guidelines of generalizable validity for the CFD simulation of Darrieus VAWTs.

## 2. Numerical Setup

### 2.1 Simulation Settings

In two previous works ([11] and [34]), the authors developed and successfully validated a two-dimensional approach to the simulation of Darrieus rotors. The aforementioned references extensively report and discuss the assessment of the main simulation settings, which are however also briefly reported here to provide a clear overview of the work to the reader.

The commercial code ANSYS Fluent [35] was used for the 2D simulations, which made use of a time-dependent unsteady Reynolds-averaged Navier-Stokes (U-RANS) approach, in the pressure based formulation. The Coupled algorithm was employed to handle the pressure-velocity coupling. The second order upwind scheme was used for the spatial discretization of the whole set of RANS and turbulence equations, as well as the bounded second order for time differencing to obtain a good resolution [11]. Air was modeled as an ideal compressible gas with standard ambient conditions, i.e. a pressure of  $1.01 \times 10^5$  Pa and a temperature of 300 K.

The global convergence of each simulation was monitored by considering the difference between the mean values of the torque coefficient over two subsequent revolutions normalized by the mean value over the second period of the pair. The periodicity error threshold was set to 0.1% [11].

Exploiting the sliding-mesh model of the solver, the simulation domain was divided into two subdomains in order to allow the rotation of the turbine, as proposed by Maître et al. [18] and Raciti Castelli et al. [19].

Concerning the turbulence closure problem, Balduzzi et al. [36], showed the effectiveness of Menter's shear stress transport (SST) [37] model in performance simulations involving unsteady aerodynamics for VAWTs, as also confirmed by the wide use in recent literature [37]. The same model was then used in the present study.

The presented CFD approach was validated against several experimental data [11]. In particular, extensive comparisons were made with experiments collected on a wind tunnel [34] by the authors.

The tested turbine was a real full-scale model of an industrial rotor with three blades and cambered airfoils, obtained by a conformal transformation of the NACA0018 section by the turbine's radius to compensate the flow curvature effects [11],[39]-[40]. The geometric features of the rotor considered in the former studies are summarized in Table 1.

With reference to this rotor, in [11] an extended sensitivity analysis was carried out on the main simulation settings. Comparative analyses assessed the influence of each numerical parameter both on the solution stability and on the accuracy with respect to purposefully collected experimental data on the study turbine. Figure 1 reports the comparison between simulated data and experiments in terms of torque coefficient of the whole turbine (three blades) to assess the capability of correctly simulating VAWT flow physics. Very good agreement is readily noticeable almost in every point of the functioning curve of the turbine. Such an impressive match between the two data sets was probably favored by the fact that the experimental data were purged from the tare torque and the blades of the rotor were long enough ( $AR > 10$ ) to reduce the influence of the tip-losses.

Moreover, in [11] the authors also demonstrated that the proposed numerical approach suitably predicted the azimuthal distribution of blade torque over a revolution of an additional literature test case.

Based on the experience of past studies, the following settings (Table 2) were proposed for this type of simulations and also endorsed for the present study:

### 2.2 Study Case

Since the work was focused on the assessment of the meshing and time-stepping strategies in order to minimize the numerical error related to the spatial and temporal discretization, the choice of the turbine to be investigated was not necessarily imposed by the availability of experimental data. A mesh-independent solution should indeed be achieved independently from experimental results [21], which can be compared only afterwards for validating purposes.

Therefore, the authors decided to perform the analysis considering a reference case represented by a hypothetical single-bladed rotor (having all other geometric features equal to those of the tested rotor presented in Table 1), where only the aerodynamic behavior of an undisturbed blade has to be solved. In this way, the interaction between different blades was not accounted for since it was thought not to be part of the main focus of the analysis. Specific attention was indeed put on a proper resolution of the flow around the

rotating airfoil in a curved flow-path. The refinement levels identified in the present study are anyhow fully compatible with those selected for the three-blade full rotor [34].

Figure 2 shows the simulation domain, where all the boundary distances are given as a function of the rotor diameter ( $D=2*R$ ). The final dimensions of both the stationary and the rotating domains were defined according to the sensitivity analysis reported in [11] in order to allow a full development of the turbine wake. The same dimensions have indeed been used successfully by the authors in similar analyses (e.g. [40]).

The velocity-inlet boundary condition is supplied by the imposition of a uniform wind profile considering an undisturbed speed of 8 m/s. The ambient pressure condition is instead imposed at the outlet boundary. A symmetry condition was finally assigned to the lateral boundaries. The symmetry condition for lateral boundaries is indeed the most common solution for this type of simulations; the authors have anyhow demonstrated in [11] that the selected width of the domain is largely sufficient not to induce any influence of the boundaries on the flow field around the turbine.

Figure 3 shows the torque characteristic prediction, obtained from the 2D CFD simulations at the conclusion of the sensitivity analysis reported in the next section. The results are here anticipated to allow the reader to understand the choices made by the authors in selecting the operating points to be analyzed.

The maximum torque output ( $c_P=0.127$ ) is produced at a TSR=3.3. Positive torque outputs, although in unstable conditions, are produced by the blade starting from TSR=1.7.

Based on previous studies establishing the necessity of defining different settings to be adopted depending on the considered operating condition [11], four different tip-speed ratios were here selected for the sensitivity analysis. In detail, two unstable conditions were considered, i.e. TSR=1.7 and TSR=2.2, in addition to the peak point (TSR=3.3) and a stable operating point (TSR=4.4), corresponding to the 75% of the maximum power output.

## 2.3 Design Points

To more clearly understand the points' selection, some details on the working conditions and flow properties are given in this section, with the goal of identifying the presence of criticalities in the physical functioning.

The instantaneous torque coefficient versus the blade angular position over a revolution ( $\theta$ ) is shown in Figure 4. Starting from the angular position of zero incidence (blade aligned with the absolute wind flow), all the four cases exhibit an increase of torque due to the increase of the blade lift, having approximately the same slope. After reaching the peak values, two different working conditions are readily distinguishable:

- The stable points (TSR=3.3 and TSR=4.4) show an uniform decrease in the second quadrant (from  $90^\circ$  to  $180^\circ$ ), followed by a constant and almost null torque extraction in the downwind section of the rotor;
- The unstable points (TSR=1.7 and TSR=2.2) show a sudden drop before  $90^\circ$ , leading to negative torque, which is caused by the decrease of the lift associated to the development of the stall.

The differences between the two conditions can be explained by comparing the vorticity field ( $\omega$ ) for all the revolution speeds. The authors consider vorticity as the most representative quantity for the determination of the level of complexity of flow structures. Indeed, high vorticity is produced when the velocity gradients are large, i.e. when the flow quantities suffer from abrupt spatial variations. To capture these structures, the size of the mesh elements must be reduced as the gradients increase.

For example, the angular position of  $\theta=140^\circ$  was analyzed in Figure 5, nearly corresponding to the location of the negative peak for TSR=1.7 and TSR=2.2. In both cases, the separation bubble gives rise to the creation of a large vortex from the leading edge. Just after this vortex has detached, a further bubble starts growing at the trailing edge. Conversely, the contours at TSR=3.3 and TSR=4.4 reveal the presence of a thickened but stable wake, indicating that the flow is still attached to the blade surface.

The vorticity level was then evaluated over the entire revolution of the blade. A dimensionless form of the vorticity ( $\tilde{\omega}$ ), divided by the rotating speed  $\Omega$ , was essential in order to be comparable throughout different operating regimes (Eq. 1):

$$\tilde{\omega} = \frac{\omega}{\Omega} \quad (1)$$

First, the maximum value of the dimensionless vorticity  $\tilde{\omega}_{max}$  reached in the overall domain was extracted, independently from the location. Figure 6 shows the trends of  $\tilde{\omega}_{max}$  as a function of the blade azimuthal position for the four TSRs. The highest intensities can be observed for the angular positions of maximum torque output for each considered case. The maximum vorticity is therefore generated in condition

of attached flow, when the lift is maximized due to the highest accelerations of the flow following the curvature of the blade profile. Thereafter, the reduction of  $\tilde{\omega}_{max}$  follows the torque decrease, with minimum values in case of vortices generation for lower revolution speeds.

At a first glance, these results may appear controversial and can lead to a misinterpretation of the phenomenon, since  $\tilde{\omega}_{max}$  decreases with the vortices onset. Actually, this outcome is due to the fact that  $\tilde{\omega}_{max}$  is a local value of a single element, but is not representative of the overall flow structures, as the extent of high-vorticity zones can be substantially altered in different operating conditions.

To overcome this aspect, the vorticity level was evaluated by means of an aggregate point of view through the calculation of the extent of the regions at high  $\tilde{\omega}$ . Conventionally, it was assumed that the vorticity is “high” when it is greater than the revolution speed by an order of magnitude, i.e. when  $\tilde{\omega} > 10$ . The area covered by the fluid regions at high vorticity was computed along the whole blade revolution and it is reported in Figure 7 in a dimensionless form  $A_{\tilde{\omega}}$  (i.e. divided by the rotor area). The trends now agree with expectations, since  $A_{\tilde{\omega}}$  increases as the torque decreases due to stall phenomena, with the highest values occurring across the 2<sup>nd</sup> and 3<sup>rd</sup> quadrants. It can be observed that the high-vorticity area grows for lower angular velocities. In particular, a marked distinction between stable and unstable operating points is clearly noticeable, with values that are more than quadrupled for the latter.

This introductory analysis was necessary to point out the modifications of the flow features throughout the operating range of the studied rotor, in order to provide some preliminary considerations for an easier comprehension of the outcomes shown in the following sections. The flow fields at low-TSR points show indeed a notably higher degree of complexity, with an oscillating torque output caused by the alternate separation of bubbles from the leading and trailing edges. It will be shown later that in these regimes the discretization requirements are stricter in order to prevent the increase of the discretization errors.

## 2.4 Meshing and time-stepping strategies

It is well known that a CFD code solves the turbulent-flow by the discretization of the continuous space and time into finite intervals. The continuous solution of the differential equations is replaced with discrete values of the variables, which are computed at only a finite number of grid points. The introduced error must be verified and minimized by systematically refining the grid size and time step.

The verification step is not equivalent to the validation step, as stated by Roache [42]. Verification means “solving the equations right” while validation means “solving the right equations”. Theoretically speaking, when the grid size and time step approach zero, the discretization error becomes negligible ensuring a correct solution of the discretized equations. Therefore, the verification consists in reducing the error to an acceptable level for the considered application. On the other hand, the suitability of the solved equations in representing the physical problem of interest is the subject of validation. The results may not be accurate because the selected models do not accurately represent the physical reality.

Once the main simulation settings have been assessed, the verification of both meshing and time-stepping strategies then becomes the key point for a successful simulation.

It is worth remarking that, in a Darrieus VAWT simulation, the sudden variation of the flow conditions on the airfoil during the revolution is responsible for a strong mutual influence between the temporal and spatial characteristic scales. To correctly reproduce a flow structure, e.g. a stall vortex, both a fine mesh (to capture the gradients) and a very small advance of the rotating frame (to avoid any undesired discontinuity of the variables between two instants) are needed. As a consequence, it might be not sufficient to perform CFD computations on a single fixed grid. A multivariate sensitivity analysis has to be carried out accounting for the mesh features and the timestep. The difference in grid size and time step between two cases should be finally sufficiently large to identify the differences in CFD results.

In the present application, the CFD domain discretization was obtained using an unstructured triangular mesh, except for the use of a structured O-grid of quadrilateral cells in the boundary layer region to improve the near wall accuracy [11]. The first cell height was imposed such as to guarantee that the  $y^+$  values from the flow solutions did not exceed the limit of the SST turbulence model, i.e.  $y^+ \sim 1$ . To ensure a high quality of the mesh near the blade, the total height of the O-grid was set to 8 mm, i.e. equal to 3% of the chord. This solution was considered adequate for the application since a boundary layer thickness of about 1.9 mm at TSR=1.7 was estimated based on the blade Reynolds number. This is indeed the most precautionary condition, since the thickness is furthermore reduced for higher revolution speeds.

Figure 8 shows the main details on the spatial discretization for the baseline and coarsest mesh (named *M1*). In the stationary domain (Figure 8a) the grid density is coarsened from the rotor to the boundaries. A

size function was set in the wake region downwind the rotor to guarantee an appropriate grid refinement. The size of the elements at the sliding interface between rotating and stationary domain is equal to  $0.1c$  on both size, corresponding to 540 nodes on the circumference (Figure 8b). Almost 550 nodes were placed on the blade surface for the  $M1$  mesh (Figure 8c), adopting a clustering in the leading and trailing edges to provide the required refinement in regions characterized by higher curvature (Figure 8d and Figure 8e). The boundary layer is discretized with an extrusion of 40 layers of quadrilateral elements, having a growth rate of 1.1. The number of nodes in which the airfoil is discretized ( $N_N$ ) is pivotal for the determination of both the attack angle of the incoming flow on the blade and the boundary layer evolution from the leading edge to the trailing edge. Moreover, the discretization level adopted in the near-blade region also controls the total number of mesh elements ( $N_E$ ), since the growth of the cell's size has to be accurately controlled. Starting from the  $M1$  setup, a node density study was performed. Four additional meshes, as illustrated in Table 3, were created in order to examine the mesh independent solution for the studied VAWT, ranging from  $1.3 \cdot 10^5$  to  $8.2 \cdot 10^5$  cells. The main parameters used to control the final mesh size were the resolution of the airfoil profile, by varying  $N_N$  and the resolution of the boundary layer, by varying progressively the rows' number of quadrilateral elements ( $N_{BL}$ ). The growth ratio of the quad layers was reduced progressively in order to keep a constant total height of about 8 mm. Figure 9 displays a detail of the boundary layer discretization at the leading edge for meshes  $M2$  to  $M5$ . The increase in the cell density is evident, since the average sizing of the elements on the blade profile ( $\Delta_B$ ) is dropped to one-fifth from the coarsest to the finest grid.

A sufficient temporal resolution is necessary to ensure an accurate unsteady simulation of the turbine. Different timestep sizes  $\Delta t$  were tested that are equivalent to specific rotational displacements along the azimuth  $\Delta\theta$ . The shortest  $\Delta t$  used was equal to 0.05 ms, corresponding to an azimuthal increment between two subsequent steps of  $0.045^\circ$  and  $0.12^\circ$  at 150 and 400 rpm respectively. The largest was 50 times bigger, i.e. 2.5 ms, corresponding to a  $\Delta\theta$  of  $2.25^\circ$  and  $6^\circ$  at 150 and 400 rpm respectively.

Globally, ten values were tested: 0.00005 s, 0.000075 s, 0.0001 s, 0.0002 s, 0.0003 s, 0.0004 s, 0.0005 s, 0.0008 s, 0.00125 s and 0.0025 s.

### 3. Sensitivity analysis results

The complete set of simulations for a full sensitivity analysis would have globally required 200 runs, resulting from the combination of four revolution speeds, five meshes and ten timesteps. Not all the combinations were however simulated. In detail, some intermediate values were not considered if the independency was already achieved. Similar considerations were also applied at high revolution speeds, where the flow conditions are more favorable and independency is soon reached, so that the shortest timesteps and the finest grid ( $M5$ ) were not used.

The assessment of the mesh and timestep independency is generally carried out in literature studies by simply monitoring the average torque (or torque coefficient) output. As an aggregate parameter, however, it could be deemed to hide differences between the simulations, due to undesired compensation between different zones of the torque profile. On this basis, the settings assessment was based both on the final average torque coefficient value ( $c_T$ ) and on an evaluation of the matching of torque profiles. This latter aspect was addressed making use of the coefficient of determination  $R^2$  [43], here defined as:

$$R^2 = 1 - \frac{\sum_{\theta=0^\circ}^{360^\circ} (c_{T@ \theta} - c_{T\_ref@ \theta})^2}{\sum_{\theta=0^\circ}^{360^\circ} (c_{T@ \theta} - c_{T\_ave})^2} \quad (2)$$

A reference case (identified as “*ref*”) was selected as the baseline model to which the torque variations can be compared. The instantaneous torque of the reference case ( $c_{Tref@ \theta}$ ) thus corresponds to the maximum refinement level for each rotating speed.  $c_{T\_ave}$  represents the average torque coefficient over a revolution at the investigated tip-speed ratio.

The criteria adopted in the identification of the independent solution are based on the following thresholds with respect to the reference case:

$$|c_{T\_ave} - c_{T\_ref\_ave}| < 0.01 \cdot c_{T\_ave\_max} \quad (3)$$

$$R^2 > 99.9\% \quad (4)$$

where the first condition imposes a difference between the average torques lower than 1% of the maximum torque at  $TSR=3.3$  (max).

### 3.1 TSR=1.7

Figure 10 illustrates the results of the sensitivity analysis at TSR=1.7 in terms of both the torque coefficient over a revolution and the coefficient of determination as a function of the global cells number, which is expressed as a ratio to the elements number of the coarsest mesh (i.e.  $N_E/N_{E,M1}$ ). The reference torque for the evaluation of the  $R^2$  is obtained with the  $M5$  mesh and the timestep of 0.00005 s, corresponding to a  $\Delta\theta$  of 0.045°.

Upon examination of Figure 10a, one could readily notice that a grid independent behavior is achieved with the  $M4$  mesh, since no remarkable variation in the average torque output is detectable with the  $M5$  refinement. The analysis in terms of  $R^2$  reveals that the matching between the torque profiles is not completely satisfactory, as also confirmed by Figure 11, where the instantaneous torque coefficient is plotted for the  $M3$ ,  $M4$  and  $M5$  meshes with analogous temporal discretization ( $\Delta t = 0.000075$  s). Especially in the second quadrant, where the torque is fluctuating due to stall, the local peaks are not perfectly corresponding in terms of both amplitude and phase. The influence of the timestep can be pointed out analyzing Figure 10a. It is readily noticeable that the results converge for a timestep less or equal to 0.000075 s, since an oscillatory convergence is detected for  $\Delta t = 0.0001$  s. A further increase of the timestep leads to an underestimation of the torque output. The  $R^2$  trends and the torque coefficient profiles of Figure 12 further demonstrate that the use of the two smallest timesteps is equivalent. A slight discrepancy can be noticed only with a 0.0001 s or greater  $\Delta t$ . In general, the influence of both the mesh and the timestep show a discontinuous behavior: the results are almost consistent when the spatial and temporal resolution is sufficiently refined. As the resolution is coarsened below a specific limit, an abrupt change in the dynamic response is observed.

### 3.2 TSR=2.2

The mesh size and timestep effects at TSR=2.2 are shown in Figure 13. The maximum refinement level was again the configuration with the  $M5$  mesh and the timestep of 0.00005 s, corresponding to an azimuthal increment  $\Delta\theta$  of 0.06°.

Focusing on the configurations with a timestep equal or greater to 0.0002 s (i.e.  $\Delta\theta = 0.24^\circ$ ), the curves of both  $c_T$  and  $R^2$  diverge as the mesh elements size is reduced. The largest timestep ensuring a grid independent behavior is 0.000075 s, and the use of the  $M4$  mesh is sufficient to guarantee a reliable estimation of the torque extraction, since the torque coefficient is perfectly predicted and  $R^2 = 99.95\%$ .

The above results clearly show that the coupling between the grid independency and the timestep independency studies is necessary, due to the mutual influence of these two parameters on the accuracy and stability of the results. It is indeed impossible to perform a mesh sensitivity analysis assuming a fixed value of the timestep: if the value is too large, it is unsuitable to establish accurate results.

Figure 14 furthermore proves that choosing the “right” mesh ( $M4$ ) with a “wrong” timestep does not allow to correctly capturing the flow structures, since the agreement of the torque extraction profiles with a timestep greater than 0.0001 s is not satisfactory. Especially in the second quadrant, the oscillation due to the stall vortices is not adequately reproduced.

### 3.3 TSR=3.3

The outcomes of the sensitivity analysis at TSR=3.3 are resumed in Figure 15. As discussed, thanks to the stable working conditions, it was here possible to avoid the use of the finest grid ( $M5$ ) and to limit the shortest tested timestep to 0.0001 s, i.e.  $\Delta\theta = 0.18^\circ$ .

As a matter of fact, the mesh and timestep independency is achieved with a lower refinement level, both in space and time. Figure 15b indicates that all cases with a temporal discretization smaller than 0.0005 s show a satisfactory matching in terms of torque distribution. Indeed, the  $R^2$  values are greater than 99.98%, largely above the tolerance threshold. Notwithstanding this, the diverging behavior of the  $c_T$  curves (Figure 15a) as the timestep increases is even more evident than the two previous analyzed cases. Using a large timestep with a fine grid ( $M4$ ) produces less accurate results than a coarse grid ( $M2$ ), since the average torque underestimation is greater and the matching between the curves is of poorer quality (lower  $R^2$ ).

The instantaneous torque coefficient curves of Figure 16, plotted for different values of  $\Delta t$  with the same mesh  $M4$ , are useful to understand the tendencies highlighted in Figure 15. By comparing the simulations with the largest and the smallest timesteps (0.0008 s and 0.0001 s respectively), one can notice that the trend is correctly reproduced (high values of  $R^2$ ), but a constant slight underestimation can be observed in the second and fourth quadrants, which is also responsible for the  $c_T$  underestimation.



### 3.4 TSR=4.4

Finally, the attention was focused on the simulations performed at the highest considered functioning condition, i.e. TSR=4.4. Analogous to TSR=3.3 case, only four mesh refinements were analyzed, from mesh *M1* to mesh *M4*, as well as the timestep was limited to 0.000075 s, corresponding to a  $\Delta\theta = 0.18^\circ$  angular timestep.

From a perusal of Figure 17, it is readily noticeable that the results are more consistent in terms of both  $c_T$  and  $R^2$ . The main difference with respect to all of the three previous cases is that this is the only working condition stable enough to achieve a mesh independent behavior independently for the timestep. The torque curves obtained with the meshes *M2*, *M3* and *M4* are almost coincident for each  $\Delta t$  considered. The differences in terms of  $R^2$  are less pronounced, therefore the configuration with *M2* and  $\Delta t = 0.0002$  s is assumed to be the optimal setup.

These aforementioned results globally show that a grid independency study must be necessarily performed accounting also for the influence of the timestep, since the azimuthal increment between two subsequent steps of analysis must be small enough to correctly describe every flow structure. Indeed, the authors showed in [11] that in a transient calculation, if a reduction of the elements size is not combined with a reduction of the timestep, the solution tends to become instable due to increase of the Courant Number (*Co*) (Eq.2):

$$Co = V \frac{\Delta t}{\Delta x} \quad (5)$$

The Courant Number expresses the ratio between the temporal timestep ( $\Delta t$ ) and the time required by a fluid particle moving with  $V$  velocity to be convected throughout a cell of dimension  $\Delta x$ .

Table 4 shows the selected mesh for each tested speed, along with the required timestep, expressed in terms of both temporal and angular increments.

To summarize the main outcomes of the analysis, it was found that the discretization requirements can be split into two different families, being the maximum torque speed approximately the boundary line. The requirements for a calculation at a revolution speed higher than the limit, i.e. in the stable part of the torque characteristic, are not extremely severe: in the present application, the grid density of the mesh *M2* (~800 nodes on the airfoil) was sufficient to guarantee accurate results and to correctly describe the torque profile if it is simulated with an angular timestep of approximately  $\Delta\theta = 0.5^\circ$ . The temporal timestep must be accordingly scaled, becoming directly proportional to the revolution speed of the rotor.

Focusing on the unstable part of the torque curve, the motion structures suffer of a sudden change, leading to the enlargement of the high-vorticity region. The intensification of velocity and pressure gradients imposes more strict requirements in terms of spatial discretization, as the mesh elements have to be small enough to capture the vortices onset. The more intense are the vortices to be captured, the finer must be the mesh, as confirmed by the necessity of adopting the *M5* mesh at TSR=1.7. The temporal discretization was found to be broadly constant and drastically reduced, resulting in values lower than  $0.1^\circ$  in terms of azimuthal increment between two steps.

## 4. Dimensionless Numbers

### 4.1 Grid-Reduced Vorticity

The findings reported in previous sections highlighted some conclusions that are of general validity in the analysis of the unsteady aerodynamics of VAWTs, i.e.:

- The intensity of the vorticity field in the region surrounding the blade increases dramatically as the rotating speed is reduced, due to the unstable working conditions;
- To avoid the increase of discretization errors, finer grids are required to correctly describe the higher gradients of the flow quantities.

Although the grid independency study was useful to assess the most suitable mesh requirements for each TSR, it is not sufficient to understand the relationship between the physical phenomena and the discretization requirements in terms of cell dimensions. In this view, the authors decided to further assess the acceptability of the selected mesh in capturing the flow structures by performing a systematic analysis of the results. More specifically, the purpose was to define a quantitative parameter to be used as an indicator of the suitability of the mesh refinement level. This parameter was deemed to correlate the flow properties, in terms

of gradients, to the mesh properties. The definition of a quantitative method in fact allows one to evaluate a priori the grid related error, without the necessity of performing an extensive and expensive analysis as the one shown in Paragraph 4.

The vorticity was considered as the most appropriate flow metric in quantifying the gradients. For 2-D flow fields it describes the rotation rate of a small fluid element about its vertical axis (Eq. 6):

$$\bar{\omega} = \left( \frac{\Delta V_y}{\Delta x} - \frac{\Delta V_x}{\Delta y} \right) \bar{k} \quad (6)$$

Vorticity at a point within a flow is zero in case of translation and linear or angular deformation, i.e. in case of potential flows. On the other hand, complex non-uniform flow patterns (shear layers, transverse flows, eddies, etc.) are characterized by nonzero vorticity. Consequently, vorticity is a physically meaningful metric for measuring these spatially varying flows.

The *Grid-Reduced Vorticity (GRV)* was introduced. The vorticity magnitude was rewritten in a dimensionless form through a proper scaling using characteristic length ( $L_0$ ) and velocity ( $V_0$ ) scales as follows (Eq. 7):

$$GRV = \frac{\omega}{V_0/L_0} = \frac{L_0}{V_0} \left( \frac{\Delta V_y}{\Delta x} - \frac{\Delta V_x}{\Delta y} \right) \quad (7)$$

Since *GRV* represents a local quantity, the local element length and the local velocity were used as length and velocity scales, respectively. The element length was chosen as a parameter representing the discretization level. The local velocity was chosen since a  $\Delta V_i$  variation has a higher relevance for the regions characterized by lower velocity.

The meaning of such a dimensionless parameter can be qualitatively explained by evaluating *GRV* for the simplified two-dimensional case of Figure 18. In the example, two adjacent square elements having the same size  $\Delta$  and a general orientation in the X-Y plane are considered. The distance between the centroids of the two elements (Eq. 8) can be expressed as:

$$\Delta = \sqrt{\Delta x^2 + \Delta y^2} \quad (8)$$

The velocity  $V_1$  in the centroid of the first element is supposed to be aligned with the centroid of the second element. The velocity  $V_2$  in the centroid of the second element differs from  $V_1$  in both directions by generic amounts  $\varepsilon_x$  and  $\varepsilon_y$  (Eq. 9).

$$\begin{cases} V_{x2} = V_{x1}(1 + \varepsilon_x) \\ V_{y2} = V_{y1}(1 + \varepsilon_y) \end{cases} \quad (9)$$

For the first centroid (Eq. 10) *GRV* can be calculated as:

$$\omega_{BB} = \frac{\Delta}{V_1} \left( \frac{\Delta V_y}{\Delta x} - \frac{\Delta V_x}{\Delta y} \right) = \frac{\Delta}{V_1} \left( \frac{V_{y2} - V_{y1}}{\Delta x} - \frac{V_{x2} - V_{x1}}{\Delta y} \right) \quad (10)$$

The elements are supposed to form a  $45^\circ$  angle with both coordinate system axes, leading to the following further simplifications (Eq. 11):

$$\begin{cases} \Delta x = \Delta y = \frac{\Delta}{\sqrt{2}} \\ V_{x1} = V_{y1} = V_1 \cos(45^\circ) = \frac{\sqrt{2}}{2} V_1 \end{cases} \quad (11)$$

$$GRV = \frac{\Delta}{V_1} \left( \frac{V_{y1}(1 + \varepsilon_y) - V_{y1}}{\frac{\Delta}{\sqrt{2}}} - \frac{V_{x1}(1 + \varepsilon_x) - V_{x1}}{\frac{\Delta}{\sqrt{2}}} \right) = \frac{\sqrt{2}}{V_1} \left( \frac{\sqrt{2}}{2} V_1 \varepsilon_y - \frac{\sqrt{2}}{2} V_1 \varepsilon_x \right) = \varepsilon_y - \varepsilon_x \quad (12)$$

The worst condition is when  $\varepsilon_y = -\varepsilon_x = \varepsilon$ , which leads to (Eq. 13):

$$GRV = 2\varepsilon \quad (13)$$

Basically, *GRV* gives an estimate of the velocity variation within a single element; therefore it represents the capability of the mesh itself of correctly computing the flow features. Under these particular

simplifications,  $GRV$  corresponds to one when a 50% velocity variation between two adjacent cells occurs. It is clear that errors in a computational cell arise when the local value of  $GRV$  is too high, while accurate results can be achieved only when  $GRV$  is substantially smaller than one. The mesh sensitivity analysis and the evaluation of  $GRV$  are therefore strictly related: grid independent results are obtained when the discretization error becomes irrelevant, i.e. when  $GRV$  is “sufficiently” small.

In order to assess the criteria for guaranteeing that the mesh refinement is “sufficient”, the results of the mesh sensitivity analysis were purposefully post-processed. The Grid-Reduced Vorticity was introduced as an additional flow quantity to be evaluated in the entire computational domain during the rotor revolution. Large  $GRV$  values were found only in the flow region surrounding the blade, due to the more complex and intense flow structures. The regions away from the moving wall are generally characterized by low gradients in relation to the size of the mesh elements.

The attention was focused on the region surrounding the blade within a distance of  $0.5c$  from the blade wall, being the more critical for the definition of the elements size and then that with the biggest impact on the discretization errors. This region normally includes the flow structures with highest vorticity such as eddies, wakes and boundary layers.

The average value of the  $GRV$  ( $GRV_{ave}$ ) was computed in the selected area for all of the tested cases. Figure 19 reports the trend of  $GRV_{ave}$  as a function of the blade azimuthal position for all of the four considered regimes with analogous discretization properties. In particular, the  $M2$  mesh was considered since it was able to provide grid independent results only for high TSR, i.e. 3.3 and 4.4. The temporal discretization does not have an influence in the present investigation; therefore, the timestep will not be specified and discussed. The figure clearly explains the reason why the  $M2$  mesh is not suitable in the case of low rotating speeds:  $GRV_{ave}$  values in the order of 0.02 imply the presence of large areas characterized by high discretization error. In roughly half of the region within a distance of  $0.5c$ , the velocity variation between two subsequent cells is greater than 1%. On the contrary, a completely different range of  $GRV_{ave}$  was obtained for  $TSR=3.3$  and  $TSR=4.4$ , since the maximum values do not exceed the limit of 0.005 and it is mostly lower than 0.003. Globally, the curves at  $TSR=1.7$  and  $TSR=2.2$  have values greater than the curves at  $TSR=3.3$  and  $TSR=4.4$  for each angular position during one revolution.

To understand the influence of different refinement levels on the results in terms of  $GRV_{ave}$ , Figure 20 shows the  $GRV_{ave}$  trend for the simulations with four different meshes (from  $M2$  to  $M5$ ) at  $TSR=1.7$ . The  $GRV_{ave}$  is reduced almost proportionally to the reduction of the average sizing of the elements on the blade profile. Using the  $M5$  mesh the values are lower than 0.005 for almost half of the revolution, with a maximum peak slightly greater than 0.01.

The  $GRV_{ave}$  trends, considering the selected mesh as indicated in Table 4 for each TSR, are displayed in Figure 21. The results are now consistent throughout the regimes, showing similar order of magnitude during the largest part of the revolution. The maximum values are limited within  $GRV_{ave}=0.01$ , which can be considered as a criterion to follow in order to estimate and reduce the source of grid-related errors.

From a theoretical point of view, the analytical solution of the system of partial differential equations is approached with a refinement of the space discretization. The choice of the degree of resolution to discretize the space is usually achieved through a grid convergence study: at least, three solutions on just as many systematically refined grids are necessary. Moreover, as shown in previous sections, space and time discretization have a mutual influence, with a notable increase in the number of runs to be carried out.

Although it is not practical to recommend in advance the most appropriate grid sizing (highly problem-dependent), the proposed approach can be useful to evaluate a priori the mesh quality.

The suggested best practice to reduce the computational effort would be to calculate  $GRV$  for an initial guess mesh, in order to be able to directly adjust the mesh size accordingly to proposed criterion. The mesh resolution should then satisfy the following requirement during the revolution (Eq. 14):

$$GRV_{ave} < 0.01 \quad (14)$$

This verification is independent of the choice of the temporal timestep and does not require an exhaustive mesh sensitivity study.

It is interesting to evaluate also the local distribution of  $GRV$ , to identify the most relevant contribution to the source of errors. For each tested speed, the attention was focused on the angular position of maximum  $GRV_{ave}$ . The local  $GRV$  values were computed in the region within a  $0.5c$  distance from the blade and the frequency distribution in terms of cumulative area was calculated and reported in Figure 22. As expected, the spatial extent of the region with  $GRV$  greater than the proposed limit of 0.01 is largest at  $TSR=1.7$ , covering

almost 40% of the area. The extension of the area at  $GRV > 0.01$  drops to almost 17% at  $TSR = 2.2$  and less than 10% at  $TSR = 3.3$  and  $4.4$ . This is the motivation of the highest peak shown in Figure 21. Notwithstanding this, the trend is inverted when considering the regions at high  $GRV$ . In particular, roughly 5% of the area is characterized by  $GRV > 0.04$  for  $TSR = 1.7$ ,  $TSR = 3.3$  and  $TSR = 4.4$ , while the area corresponds to 10% for  $TSR = 2.2$ . Moving to the extreme, the area at  $GRV = 0.2$  is lower than 0.05% at  $TSR = 1.7$  and  $TSR = 2.2$ , while is in the order of 0.15% at  $TSR = 3.3$  and  $TSR = 4.4$ .

In addition, Figure 23 shows the  $GRV$  field for the same cases depicted in Figure 5. For each rotating speed, the results are displayed considering the final configuration mesh. Analogous levels of  $GRV$  can be observed throughout the different regimes, whereas the vorticity levels of Figure 5 were not consistent. In more detail, although the highest vorticity magnitude was observed in the wake region for  $TSR = 3.3$  and  $TSR = 4.4$ , the reduced element size in proximity of the blade wall guarantees low  $GRV$  values. On the contrary, the vorticity magnitude of the large eddy originated from the leading edge at  $TSR = 1.7$  is substantially lower but the greater local length of the mesh elements leads to almost equal  $GRV$  levels.

Therefore, it is clear that the main issue for a correct computation of the flow structures at low  $TSRs$  is to generate a computational grid characterized by small element size in a wide region surrounding the blade, in order to include the detaching vortices. Conversely, at high  $TSRs$  is sufficient to accurately discretize the boundary layer and the wake region. In particular, Figure 24 shows that the peaks of  $GRV$  at  $TSR = 3.3$  are located on the leading edge, where the acceleration of the flow is maximum, and downstream the leading edge.

Finally, Figure 25 reports the  $GRV$  field at  $TSR = 1.7$  for eight different azimuthal positions along a complete rotor revolution. The second and third quadrants are the most critical for an accurate resolution since the dynamic stall phenomena involve large regions with significant gradients. Therefore, the grid coarsening with respect to the wall-closest grid is responsible of high values of  $GRV$  at distances even greater than one chord from the blade surface.

## 4.2 Courant Number

Once the spatial discretization has been assessed based on the analysis of the  $GRV$ , the proper timestep must be identified for each  $TSR$ , in order to ensure accurate results of the unsteady simulations. As discussed by the authors in two previous works ([11] and [34]), the Courant number ( $Co$ ) analysis can provide the correct guideline for this selection. Based on its formulation (Eq. 5), this number expresses the ratio between the temporal timestep ( $\Delta t$ ) and the time required by a fluid particle moving with  $V$  velocity to be convected throughout a cell of dimension  $\Delta x$ .

While in case of explicit schemes for temporal discretization the Courant-Friedrichs-Lewy (CFL) criterion imposes a limit on the maximum allowed value of  $Co$  (i.e.  $Co < 1$  [44]-[46]) to ensure the stability of the calculation, implicit methods are thought to be unconditionally stable with respect to the timestep size [25]. Although theoretically valid if the problem is studied with a linear stability analysis, when the timestep is increased non-linearity effects would become prominent and oscillatory solutions may occur. On these bases, the literature indicates that an operational  $Co$  between 5 and 10 for viscous turbomachinery flows, solved with an implicit scheme, provides the best error damping properties ([45] and [46]).

According to Balduzzi et al. [11], in case of Darrieus VAWTs a specific analysis is suggested on the Courant Number conditions in proximity of the blades, as a correct description of the flow in these zones is in fact deemed to be the most restrictive requisite to accurately predict the torque output of the rotor.

As a general remark, the results of Table 4 highlighted that remarkably finer meshes are needed as long as the  $TSR$  is reduced, in order to correctly capture the intensity and the extension of strong-gradients zones in the flow. According to Eq. 5, in order to contain the Courant Number it has to be expected that the also the timestep has to be reduced with  $TSR$ .

In particular, in order to define some general guidelines for the time-stepping strategy, a reference Courant Number ( $Co^*$ ) has been here defined, assuming that in Eq. 5 the reference length is represented by the average nodes distance along the airfoil and the reference velocity is the peripheral speed of the airfoil.

Based on the present definition, Table 5 reports the resulting  $Co^*$  for the four investigated  $TSRs$  using the final settings obtained by the sensitivity analysis.

Upon examination of the table, it is worth noticing that a clear trend was highlighted. In particular, at low  $TSRs$ , in which the presence of strong gradients makes the resolution requirements more strict, the  $Co^*$  must be contained in the order of 5, whereas an increase up to approximately 10 can be tolerated at higher  $TSRs$ , where the flow is mainly attached.

In detail, the  $Co^*$  reduction at unstable regimes is mainly due to the onset of flow phenomena at multiple frequencies (e.g. vortices detaching from the blades in the 2<sup>nd</sup> and 3<sup>rd</sup> quadrants), which therefore require a different temporal resolution. For example, in Figure 26 the vorticity contours of a blade at TSR=2.2 between  $\theta=114.3^\circ$  and  $\theta=157.5^\circ$  are displayed consequently.

From Figure 26, it is apparent that, for high AoAs, the blade starts experiencing a vortex shedding quite similar to that of a bluff body. In the present case, a characteristic frequency of approximately 14 Hz (corresponding to a period of 0.07 s) was noticed both at TSR=1.7 and at TSR=2.2.

It was here then supposed that the required timestep reduction was mainly needed to correctly describe this additional phenomenon, which introduced a frequency notably higher than the revolution speed. The selected timestep of 0.000075 s, in particular, allowed the description of each single vortex shedding cycle with approximately 1000 timesteps, which are in perfect agreement with the best literature prescriptions (e.g. [47]).

As a final remark, the selection of the proper Courant Number (or  $Co^*$ ), however, requires a specific attention. In general, the  $Co$  should indeed be reduced as far as possible. Low Courant numbers can be, however, easily achieved by increasing the element size ( $\Delta x$  in Eq. 5), but the coarsening of the mesh is thought, on the other hand, to worsen the accuracy of the simulation. A time-step selection based on the  $Co^*$  must therefore be carried out only after the mesh requirements definition, e.g. based on the  $GRV$ .

## 5. Conclusions

In the paper, a systematic analysis has been carried out to define a robust strategy for the assessment of the meshing and time-stepping requirements in the CFD simulation of a Darrieus wind turbine. The spatial and temporal discretization are indeed two of the most crucial sources of numerical error, due to the difference between the exact solution of the analytical system of partial differential equations and the numerical solution obtained with finite discretization. In the case of vertical-axis wind turbines, the proper selection of the discretization strategy is even more complex because different aerodynamic phenomena have to be described depending on the tip-speed ratio.

A study-case having a single blade was first derived from a real rotor, which was successfully simulated in the past and verified with experiments. The optimal settings in terms of mesh and timestep were then defined by means of a cross-coupled sensitivity analysis, which was pushed up to the physical limits of the problem with no limitations imposed by the computing resources. Four functioning regimes were investigated, corresponding to tip-speed ratios of 1.7, 2.2, 3.3 and 4.4.

Once the optimized settings for each TSR were defined, the computed flow fields were analyzed to understand the main challenging phenomena for the simulation assessment. In particular, the extension and intensity of high-vorticity zones were supposed to be the most requiring elements for the mesh refinement.

To verify this assumption, a dimensionless number was proposed, representing a dimensionless expression of vorticity. Based on its definition,  $GRV$  in fact quantifies the velocity variation between two cells. This new dimensionless number, calculated for different zones of the flow field, showed that low TSR regimes are characterized by higher levels of vorticity in a larger part of the flow around the blades. In order to describe correctly the gradients in those zones, finer meshes are therefore required. In particular, upon comparison of the four optimal settings, it was found that average  $GRV$  within a proper mesh should be not higher than 0.01 (i.e.  $GRV_{ave} < 0.01$ ), corresponding to a maximum velocity variation between two adjacent cells of  $5 \cdot 10^{-3}$ .

Once the mesh requirements have been assessed using the proposed criterion, the selection of the proper timestep was again connected to the definition of the dimensionless number  $Co^*$ , i.e. a generalized version of the Courant number based on the average elements length on the airfoil and the peripheral speed. Consistency was again found between the results, highlighting the need of smaller timesteps at low TSRs, where the presence of largely separated regions becomes more frequent. In particular, it was found that the optimal timestep was that ensuring approximately 1000 points within the period of the vortex shedding established on the blades for high AoAs in the second and third quadrants of the turbine.

In conclusion, the integrated approach presented in the paper, based on dimensionless numbers, is thought to allow the assessment of the mesh and timestep requirements in the CFD simulation of a Darrieus wind turbine. In this view, it is supposed to provide in the near future an important contribution to the numerical analyses on these machines by setting a standard for these simulations and contemporarily reducing the computational costs due to the preliminary sensitivity analyses.

## 6. Acknowledgments

Thanks are due to Prof. Ennio Antonio Carnevale of the University of Florence for his support in this study.

## 7. Nomenclature

### Acronyms

|        |  |
|--------|--|
| AR     | Aspect Ratio                             |
| CFD    | Computational Fluid Dynamics             |
| CFL    | Courant, Friedrichs and Levy criterion   |
| GCI    | Grid Convergence Index                   |
| GRE    | General Richardson Extrapolation         |
| SST    | Shear Stress Transport                   |
| U-RANS | Unsteady Reynolds-Averaged Navier-Stokes |
| VAWT   | Vertical-Axis Wind Turbine               |

### Greek symbols

|                  |   |                        |
|------------------|---|------------------------|
| $\Delta$         | Cell Dimension                                      | [m]                    |
| $\Delta_B$       | Average sizing of the elements on the blade profile | [m]                    |
| $\Delta\theta$   | Azimuthal Angle Increment                           | [deg]                  |
| $\Delta t$       | Temporal Timestep                                   | [s]                    |
| $\varepsilon$    | Velocity Variation                                  |                        |
| $\vartheta$      | Azimuthal Angle                                     | [deg]                  |
| $\sigma$         | Turbine's Solidity                                  |                        |
| $\omega$         | Vorticity   | [s <sup>-1</sup> ]     |
| $\tilde{\omega}$ | Dimensionless Vorticity                             |                        |
| $\Omega$         | Revolution Speed                                    | [rad s <sup>-1</sup> ] |

### Latin symbols

|                      |  |       |
|----------------------|--|-------|
| $A_{\tilde{\omega}}$ | Dimensionless High Vorticity Area                  |       |
| $c$                  | Blade's Chord                                      | [c]   |
| $c_T$                | Torque Coefficient                                 |       |
| $c_P$                | Power Coefficient                                  |       |
| $Co$                 | Courant's Number                                   |       |
| $Co^*$               | Reference Courant Number Based on Peripheral Speed |       |
| $y^+$                | Dimensionless Wall Distance                        |       |
| $D$                  | Turbine's Diameter                                 | [m]   |
| $GRV$                | Grid-Reduced Vorticity                             |       |
| $L_0$                | Length Scale                                       | [m]   |
| $N_{BL}$             | Number of layers in the boundary layer             |       |
| $N_N$                | Number of nodes on blade profile                   |       |
| $N_E$                | Total number of mesh elements                      |       |
| $R$                  | Turbine's Radius                                   |       |
| $R^2$                | Coefficient of determination                       |       |
| TSR                  | Tip-Speed Ratio                                    |       |
| $V$                  | Velocity   | [m/s] |
| $V_0$                | Velocity Scale                                     | [m/s] |

## 8. References

- [1] M.H. Mohamed, Performance investigation of H-rotor Darrieus turbine with new airfoil shapes, Energy, Volume 47, Issue 1, November 2012, Pages 522-530, ISSN 0360-5442, <http://dx.doi.org/10.1016/j.energy.2012.08.044>.

- [2] Balduzzi F, Bianchini A, Carnevale EA, Ferrari L, Magnani S. Feasibility analysis of a Darrieus vertical-axis wind turbine installation in the rooftop of a building. *Applied Energy* 2012;97:921–929.
- [3] Willy Tjiu, Tjukup Marnoto, Sohif Mat, Mohd Hafidz Ruslan, Kamaruzzaman Sopian, Darrieus vertical axis wind turbine for power generation I: Assessment of Darrieus VAWT configurations, *Renewable Energy*, Volume 75, March 2015, Pages 50-67, ISSN 0960-1481, <http://dx.doi.org/10.1016/j.renene.2014.09.038>.
- [4] Willy Tjiu, Tjukup Marnoto, Sohif Mat, Mohd Hafidz Ruslan, Kamaruzzaman Sopian, Darrieus vertical axis wind turbine for power generation II: Challenges in HAWT and the opportunity of multi-megawatt Darrieus VAWT development, *Renewable Energy*, Volume 75, March 2015, Pages 560-571, ISSN 0960-1481, <http://dx.doi.org/10.1016/j.renene.2014.10.039>.
- [5] Mazharul Islam, David S.-K. Ting, Amir Fartaj, Aerodynamic models for Darrieus-type straight-bladed vertical axis wind turbines, *Renewable and Sustainable Energy Reviews*, Volume 12, Issue 4, May 2008, Pages 1087-1109, ISSN 1364-0321, <http://dx.doi.org/10.1016/j.rser.2006.10.023>.
- [6] Paraschivoiu I, *Wind Turbine Design with Emphasis on Darrieus Concept*. Polytechnic International Press, Canada; 2002.
- [7] Paraschivoiu I, *Wind Turbine Design with Emphasis on Darrieus Concept*. Polytechnic International Press, Canada; 2002.
- [8] Bianchini A, Ferrari L, Magnani S. Start-up behavior of a three-bladed h-Darrieus VAWT: experimental and numerical analysis. *Proc. of the ASME Turbo Expo 2011, Vancouver (Canada)*, June 6-10; 2011.
- [9] Paraschivoiu I, Delclaux F. Double Multiple Streamtube Model with Recent Improvements. *Journal of Energy* 1983;7(3):250-255.
- [10] Alessandro Bianchini, Giovanni Ferrara, Lorenzo Ferrari, Design guidelines for H-Darrieus wind turbines: Optimization of the annual energy yield, *Energy Conversion and Management*, Volume 89, 1 January 2015, Pages 690-707, ISSN 0196-8904, <http://dx.doi.org/10.1016/j.enconman.2014.10.038>.
- [11] Balduzzi, F., Bianchini, A., Maleci, R., Ferrara, G. and Ferrari, L., 2013, "Critical issues in the CFD simulation of Darrieus wind turbines," paper under publication in *Renewable Energy*.
- [12] Marco Raciti Castelli, Alessandro Englaro, Ernesto Benini, The Darrieus wind turbine: Proposal for a new performance prediction model based on CFD, *Energy*, Volume 36, Issue 8, August 2011, Pages 4919-4934, ISSN 0360-5442, <http://dx.doi.org/10.1016/j.energy.2011.05.036>.
- [13] M.H. Mohamed, Aero-acoustics noise evaluation of H-rotor Darrieus wind turbines, *Energy*, Volume 65, 1 February 2014, Pages 596-604, ISSN 0360-5442, <http://dx.doi.org/10.1016/j.energy.2013.11.031>.
- [14] Al-Shammari, E.T., Amirmojahedi, M., Shamshirband, S., Petković, D., Pavlović, N.T., Bonakdari, H., 2015, "Estimation of wind turbine wake effect by adaptive neuro-fuzzy approach," *Flow Measurement and Instrumentation*, **45**(October 2015), pp.1-6. DOI: 10.1016/j.flowmeasinst.2015.04.002
- [15] Petkovića, D., Shamshirband, S., Anuar, N.B., Saboo, H., Wahab, A.W.A., Protić, M., Zalnezhad, E., Mirhashemi, S.M.A., 2014, "An appraisal of wind speed distribution prediction by soft computing methodologies: A comparative study," *Energy Conversion and Management*, **84**(October 2014), pp.133-139.
- [16] D.C. Wilcox, *Turbulence Modeling for CFD*, DCW Industries Inc., La Canada (CA), 1998.
- [17] A. Rossetti, G. Pavesi, Comparison of different numerical approaches to the study of the H-Darrieus turbines start-up, *Renewable Energy*. 50 (2013) 7-19.
- [18] T. Maître, E. Amet, C. Pellone, Modeling of the flow in a Darrieus water turbine: Wall grid refinement analysis and comparison with experiments, *Renewable Energy*. 51 (2013) 497-512.
- [19] M. Raciti Castelli, G. Ardizzon, L. Battisti, E. Benini, G. Pavesi, Modeling strategy and numerical validation for Darrieus vertical axis micro-wind turbine, *Proceedings of the ASME IMECE 2010, Vancouver, Canada*, November 12-18, 2010.
- [20] L. A. Danao, J. Edwards, O. Eboibi, R. Howell, A numerical investigation into the influence of unsteady wind on the performance and aerodynamics of a vertical axis wind turbine, *Applied Energy*, Volume 116, 1 March 2014, Pages 111-124, ISSN 0306-2619, <http://dx.doi.org/10.1016/j.apenergy.2013.11.045>.
- [21] K.M. Almohammadi, D.B. Ingham, L. Ma, M. Pourkashan, Computational fluid dynamics (CFD) mesh independency techniques for a straight blade vertical axis wind turbine, *Energy*, Volume 58, 1 September 2013, Pages 483-493, ISSN 0360-5442, <http://dx.doi.org/10.1016/j.energy.2013.06.012>
- [22] E. Amet, T. Maître, C. Pellone, J. L. Achard, 2D Numerical Simulations of Blade-Vortex Interaction in a Darrieus Turbine, *J. Fluids Eng.* 131 11 (2009) 1-15, doi:10.1115/1.4000258

- 711 [23] R. Nobile, M. Vahdati, J. F. Barlow, A. Mewburn-Crook, Unsteady flow simulation of a vertical axis  
712 augmented wind turbine: A two-dimensional study, *Journal of Wind Engineering and Industrial*  
713 *Aerodynamics*, 125 (2014) 168-179, ISSN 0167-6105, <http://dx.doi.org/10.1016/j.jweia.2013.12.005>.
- 714 [24] C.J. Simao Ferreira, H. Bijl, G. van Bussel, G. van Kuik, Simulating Dynamic Stall in a 2D VAWT:  
715 Modeling strategy, verification and validation with Particle Image Velocimetry data, *Journal of Physics.*  
716 *Conf. Series* 75 (1), 012023.
- 717 [25] S. Lain, C. Osorio, Simulation and evaluation of a straight-bladed Darrieus-type cross flow marine  
718 turbine, *Journal of Scientific & Industrial Research*. 69 (2010) 906-912.
- 719 [26] Untaroiu, H. G. Wood, P. E. Allaire, R. J. Ribando, Investigation of Self-Starting Capability of Vertical  
720 Axis Wind Turbines Using a Computational Fluid Dynamics Approach, *Journal of Solar Energy*  
721 *Engineering*. 133 4 (2011) 1-8.
- 722 [27] R. Gupta, S. Roy, A. Biswas, Computational fluid dynamics analysis of a twisted airfoil shaped two-  
723 bladed H-Darrieus rotor made from fibreglass reinforced plastic (FRP), *International Journal of Energy*  
724 *and Environment*, 1 6 (2010) 953-968.
- 725 [28] L. Daroczy, M. H. Mohamed, G. Janiga, D. Thevenin, Analysis of the Effect of a Slotted Flap  
726 Mechanism on the Performance of an H-Darrieus Turbine Using CFD, *Proceedings of the ASME Turbo*  
727 *Expo 2014*, Düsseldorf, Germany, June 16-20, 2014.
- 728 [29] F. Trivellato, M. Raciti Castelli, On the Courant–Friedrichs–Lewy criterion of rotating grids in 2D  
729 vertical-axis wind turbine analysis, *Renewable Energy*, Volume 62, February 2014, Pages 53-62, ISSN  
730 0960-1481, <http://dx.doi.org/10.1016/j.renene.2013.06.022>
- 731 [30] I.B. Celik, U. Ghia, P. J. Roache, C.J. Freitas, H. Coleman, P. E. Raad, Procedure for Estimation and  
732 Reporting of Uncertainty due to Discretization in CFD Applications, *Journal of Fluids Engineering*  
733 (Special Publication), Vol. 130 7 (2008) 1-4, doi:10.1115/1.2960953
- 734 [31] C. J. Roy, Review of code and solution verification procedures for computational simulation, *Journal of*  
735 *Computational Physics*. 205 1 (2005) 131-156.
- 736 [32] T. S. Phillips, C. J. Roy, Evaluation of Extrapolation-Based Discretization Error and Uncertainty  
737 Estimators, *AIAA Paper 2011-215*, 49th AIAA Aerospace Sciences, Orlando, Florida, January 4-7,  
738 2011.
- 739 [33] F. Stern; R. Wilson, J. Shao, Quantitative V&V of CFD simulations and certification of CFD codes, *Int.*  
740 *J. Numer. Meth. Fluids*, 50 11 (2006) 1335–1355, doi: 10.1002/fld.1090.
- 741 [34] Balduzzi, F., Bianchini, A., Maleci, R., Ferrara, G. and Ferrari, L., 2015, “Blade design criteria to  
742 compensate the flow curvature effects in H-Darrieus wind turbines,” *Journal of Turbomachinery*,  
743 **137**(1), pp. 1-10.
- 744 [35] Ansys, Inc., 2013, *Fluent Theory Guide*, release 14.5. 4.
- 745 [36] Balduzzi F, Bianchini A, Gigante FA, Ferrara G, Campobasso MS, Ferrari L, Parametric and  
746 Comparative Assessment of Navier-Stokes CFD Methodologies for Darrieus Wind Turbine  
747 Performance Analysis. *Proc. of the ASME Turbo Expo 2015*, Montreal, Canada, June 15-19, 2015. DOI:  
748 10.1115/GT2015-42663
- 749 [37] F.R. Menter, Two-Equation Eddy-Viscosity Turbulence Models for Engineering Applications. *AIAA J.*  
750 1994;32(8):1598–1605.
- 751 [38] László Daróczy, Gábor Janiga, Klaus Petrasch, Michael Webner, Dominique Thévenin, Comparative  
752 analysis of turbulence models for the aerodynamic simulation of H-Darrieus rotors, *Energy*, Available  
753 online 24 August 2015, ISSN 0360-5442, <http://dx.doi.org/10.1016/j.energy.2015.07.102>.
- 754 [39] Bianchini A, Balduzzi F, Rainbird J, Peiro J, Graham JMR, Ferrara G, Ferrari L, An Experimental and  
755 Numerical Assessment of Airfoil Polars for Use in Darrieus Wind Turbines. Part 1 - Flow Curvature  
756 Effects. *Journal of Engineering for Gas Turbines and Power* 2016;138(3). DOI: 10.1115/1.4031269.
- 757 [40] Bianchini, A., Balduzzi, F., Rainbird. J., Peiro, J., Graham, J.M.R., Ferrara, G. and Ferrari, L., On the  
758 Influence of Virtual Camber Effect on Airfoil Polars for Use in Simulations of Darrieus Wind Turbines.  
759 *Energy Conversion and Management* 2015;**106**(December 2015):373-384.  
760 DOI: 10.1016/j.enconman.2015.09.053
- 761 [41] Bianchini, A., Ferrara, G. and Ferrari, L., Pitch Optimization in Small-size Darrieus Wind Turbines.  
762 *Energy Procedia* 2015;81(December 2015):122–132. DOI:10.1016/j.egypro.2015.12.067
- 763 [42] P.J. Roache, Quantification of uncertainty in Computational Fluid Dynamics. *Annu. Rev. Fluid. Mech.*  
764 29 (1997) 123–160
- 765 [43] J. Mandel, *The Statistical Analysis of Experimental Data*, Dover Publications, New York (USA), 1984.
- 766 [44] J. Ferziger, M. Peric, *Computational Methods for Fluid Dynamics*, 3rd rev, Springer, Berlin, 2002.

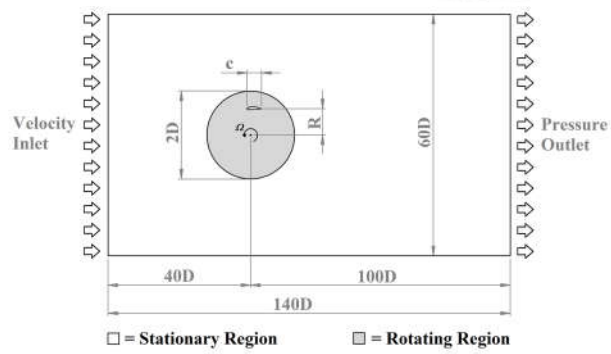
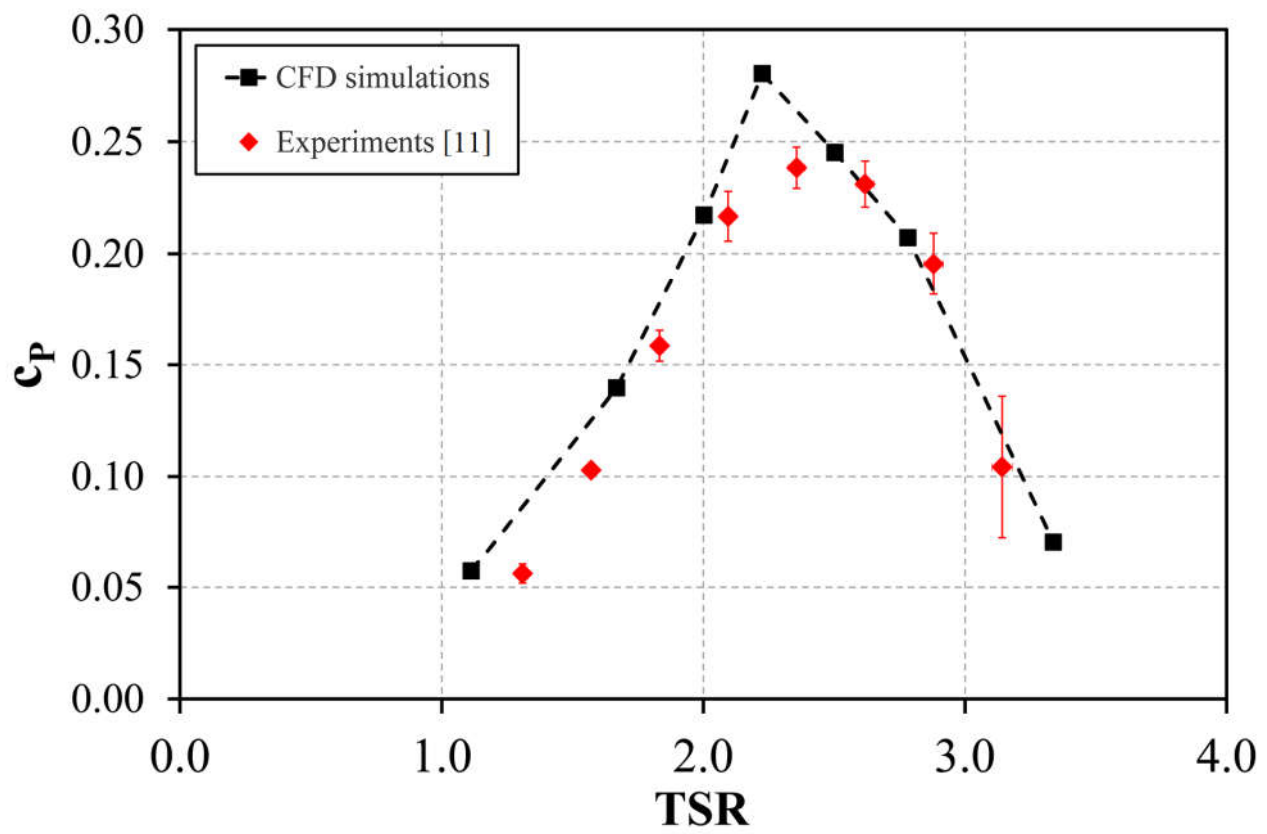


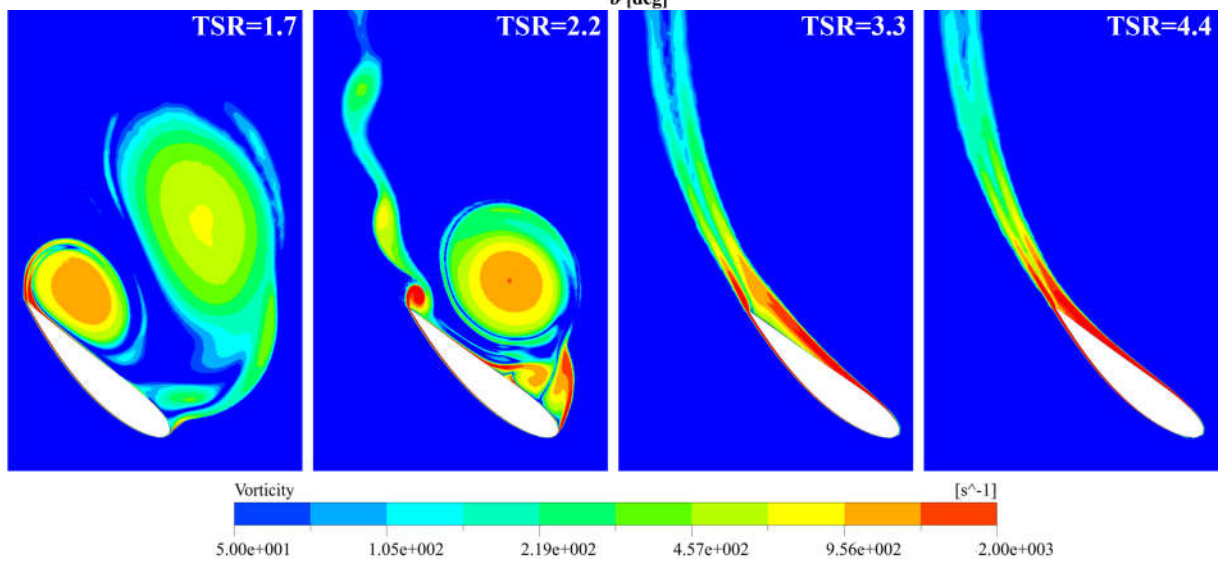
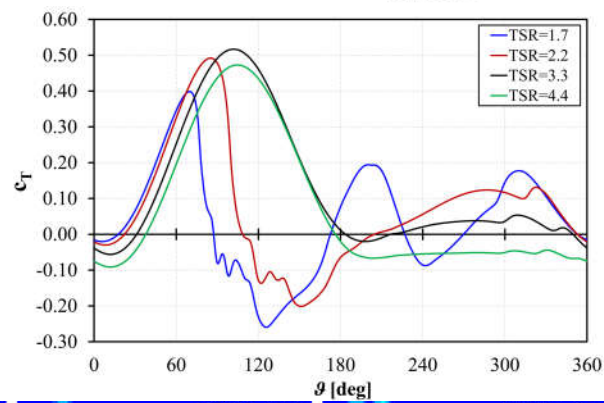
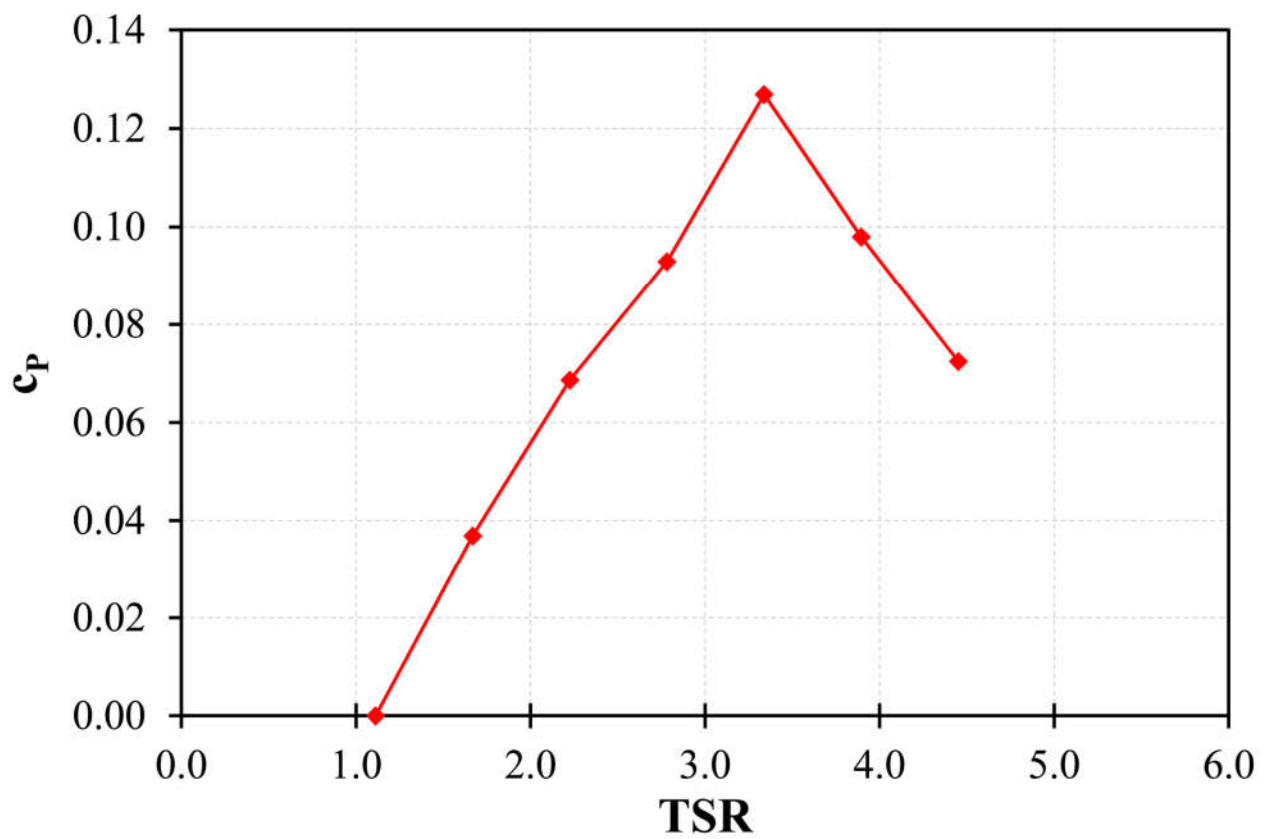
767 [45] R.S. Amano, B. Sunden, Computational Fluid Dynamics and Heat Transfer: Emerging Topics, WIT  
768 Press, Southampton, UK, 2011.

769 [46] C.J. Hearn, The Dynamics of Coastal Models, Cambridge University Press, Cambridge, UK, 2008.

770 [47] Cox, J.A., Brentner, K.S. and Rumsey, C.L., 1998, "Computation of Vortex Shedding and Radiated  
771 Sound for a Circular Cylinder: Subcritical to Transcritical Reynolds Numbers," *Theoret. Comput. Fluid*  
772 *Dynamics*, **12**, pp. 233–253.

773  
774  
775  
776  
777  
778  
779  
780  
781  
782  
783  
784  
785  
786  
787  
788  
789  
790  
791  
792  
793  
794  
795  
796  
797  
798  
799  
800  
801  
802  
803  
804  
805  
806  
807  
808  
809  
810  
811  
812  
813  
814  
815  
816  
817  
818  
819  
820  
821  
822

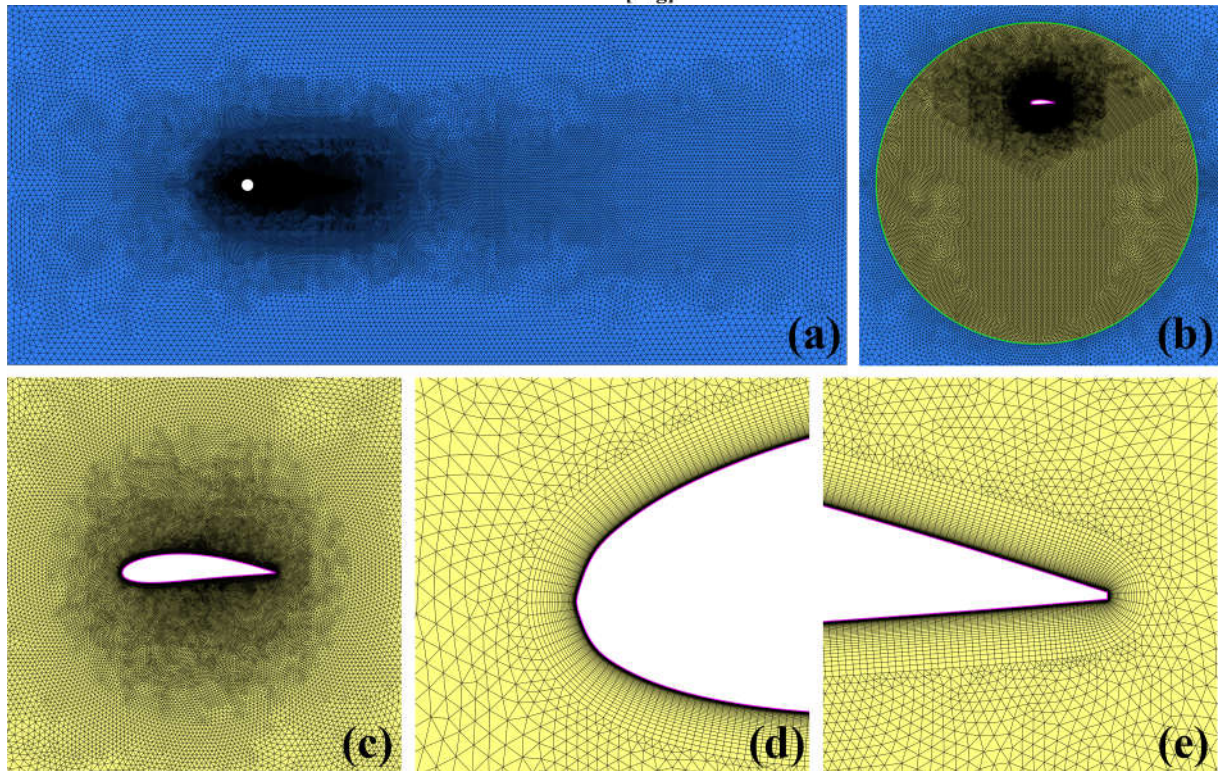
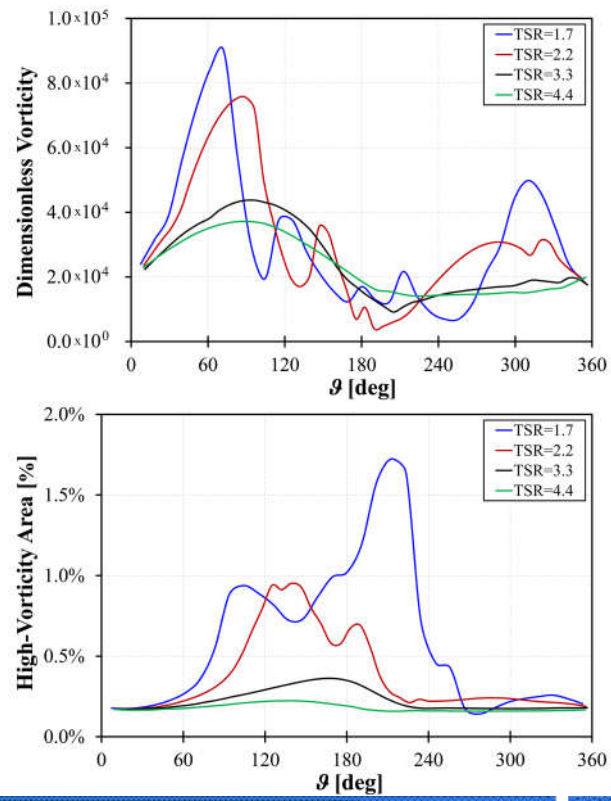


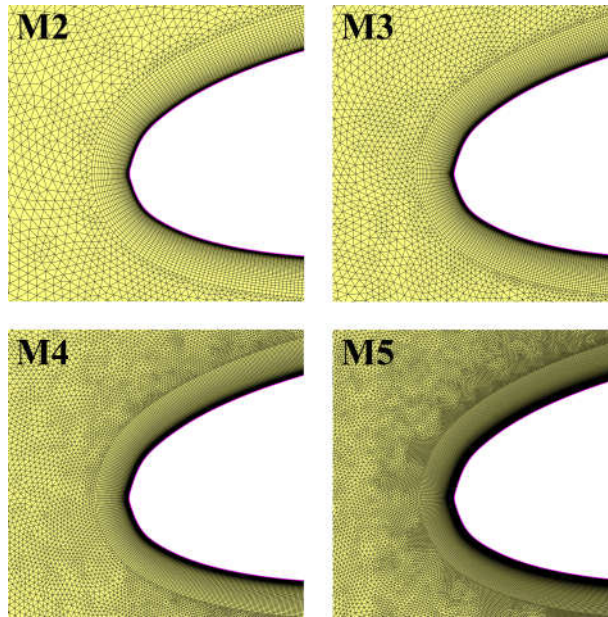


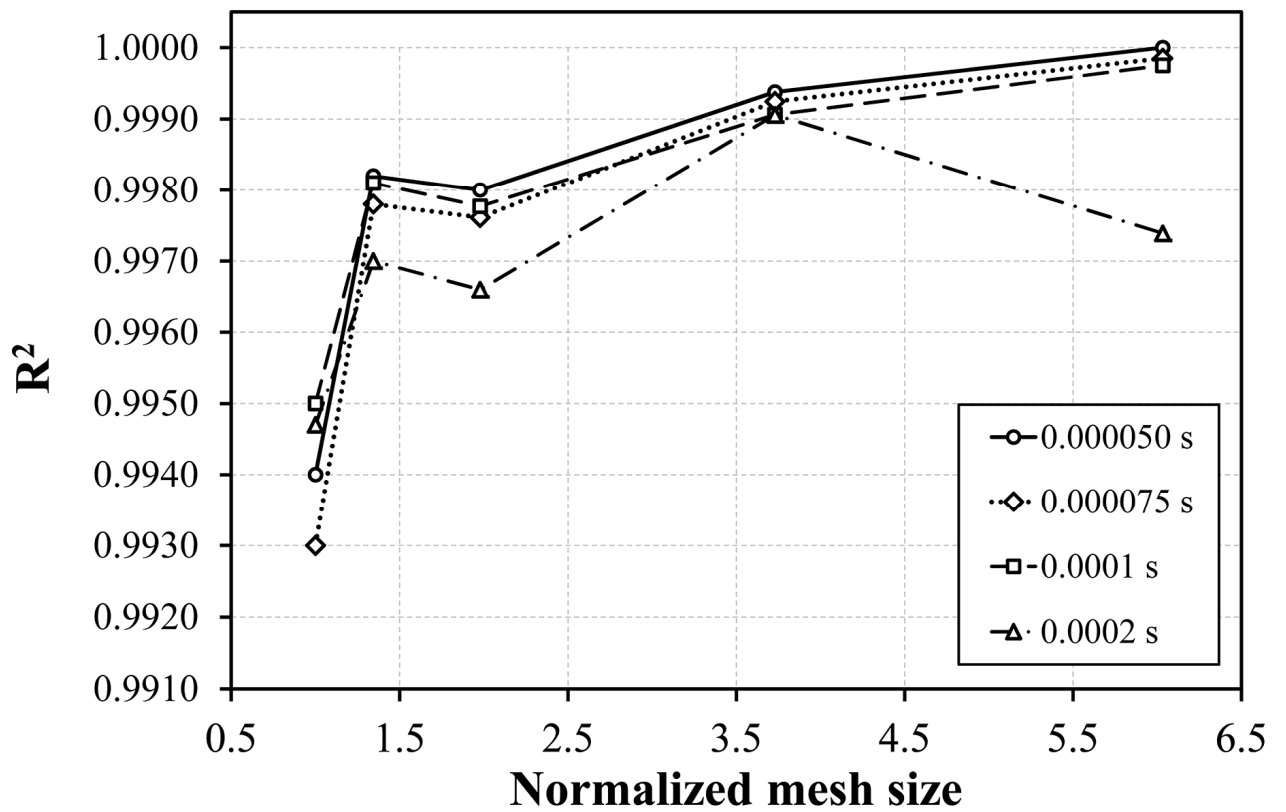
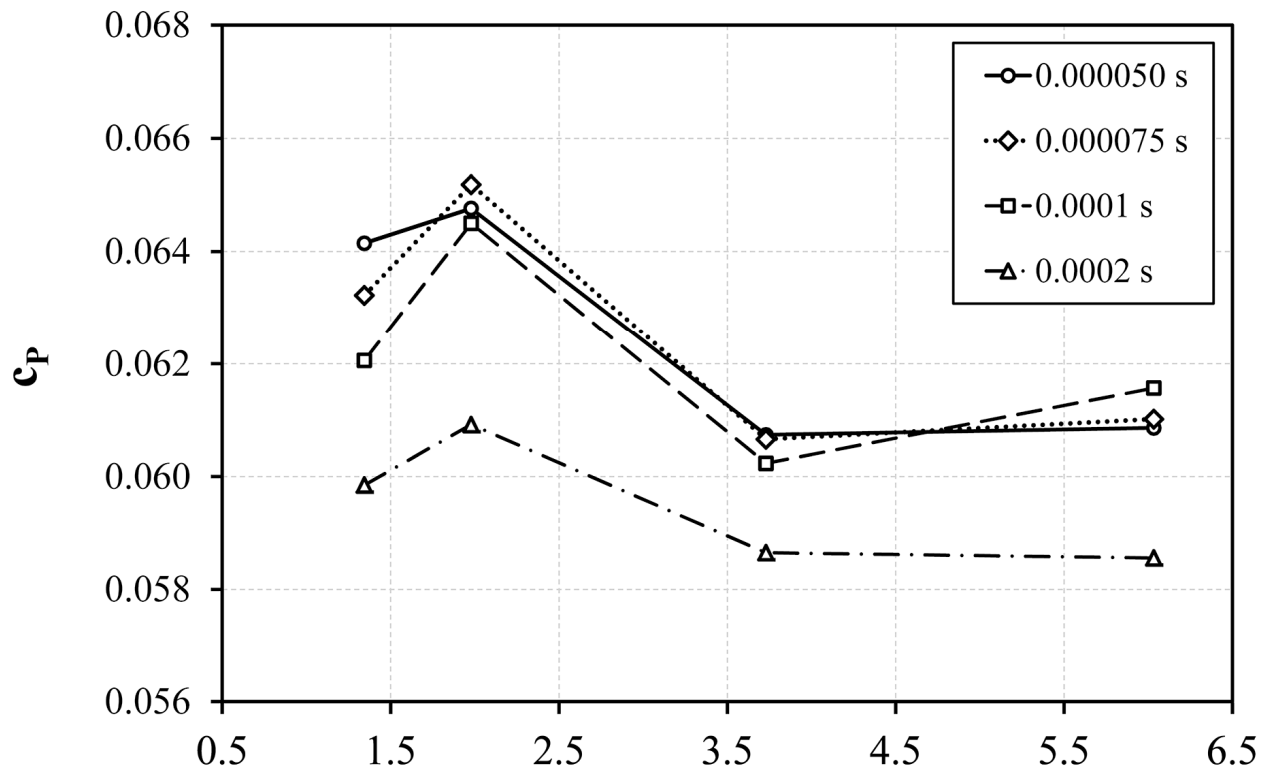
828

829

830

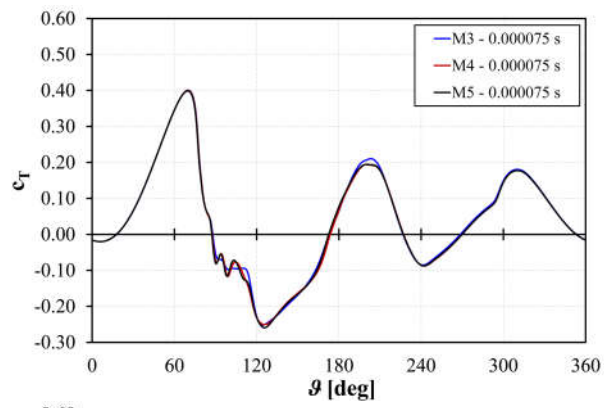




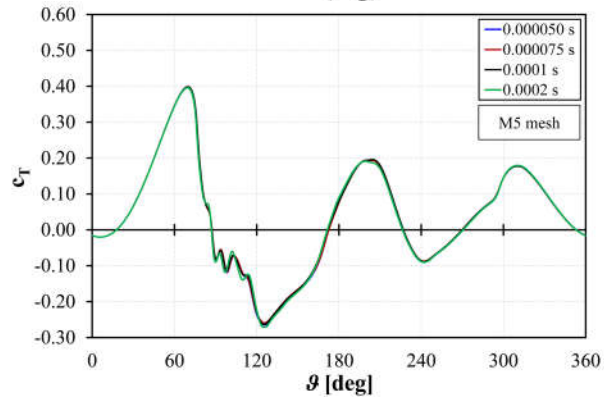


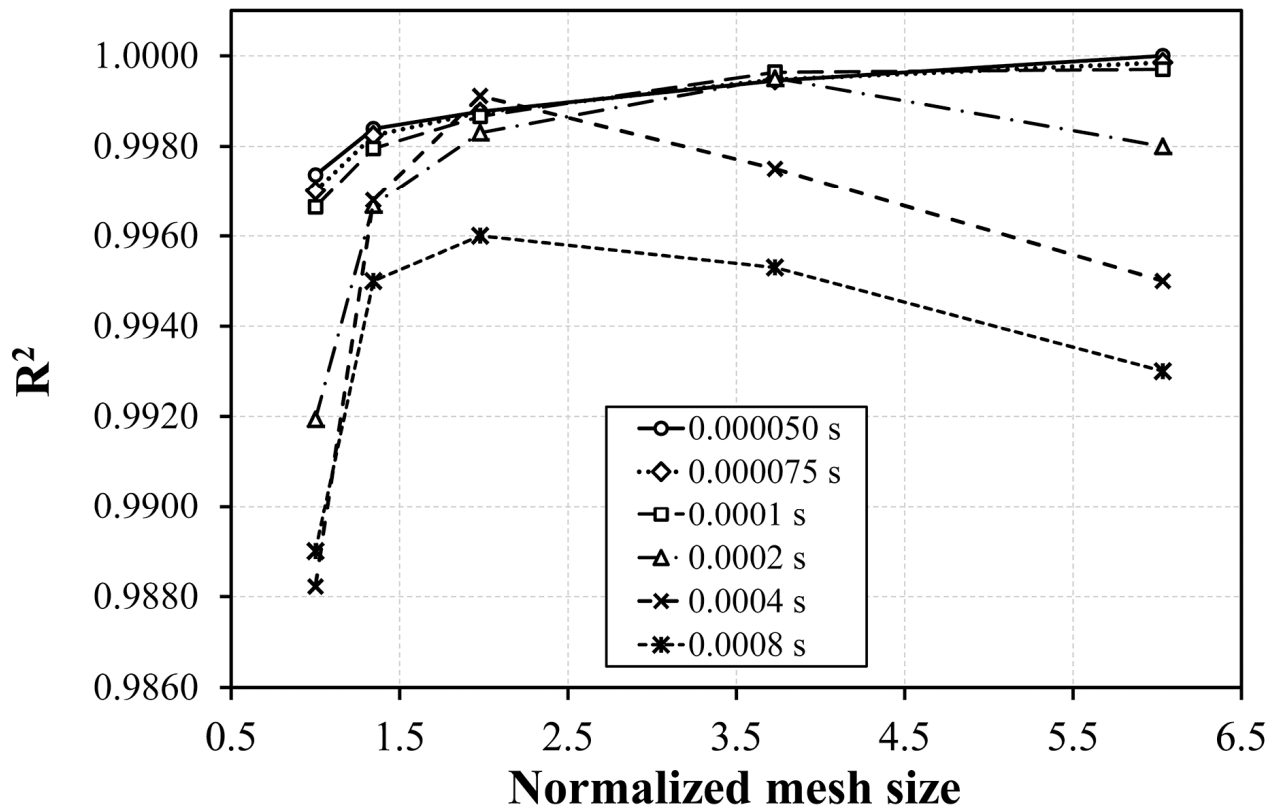
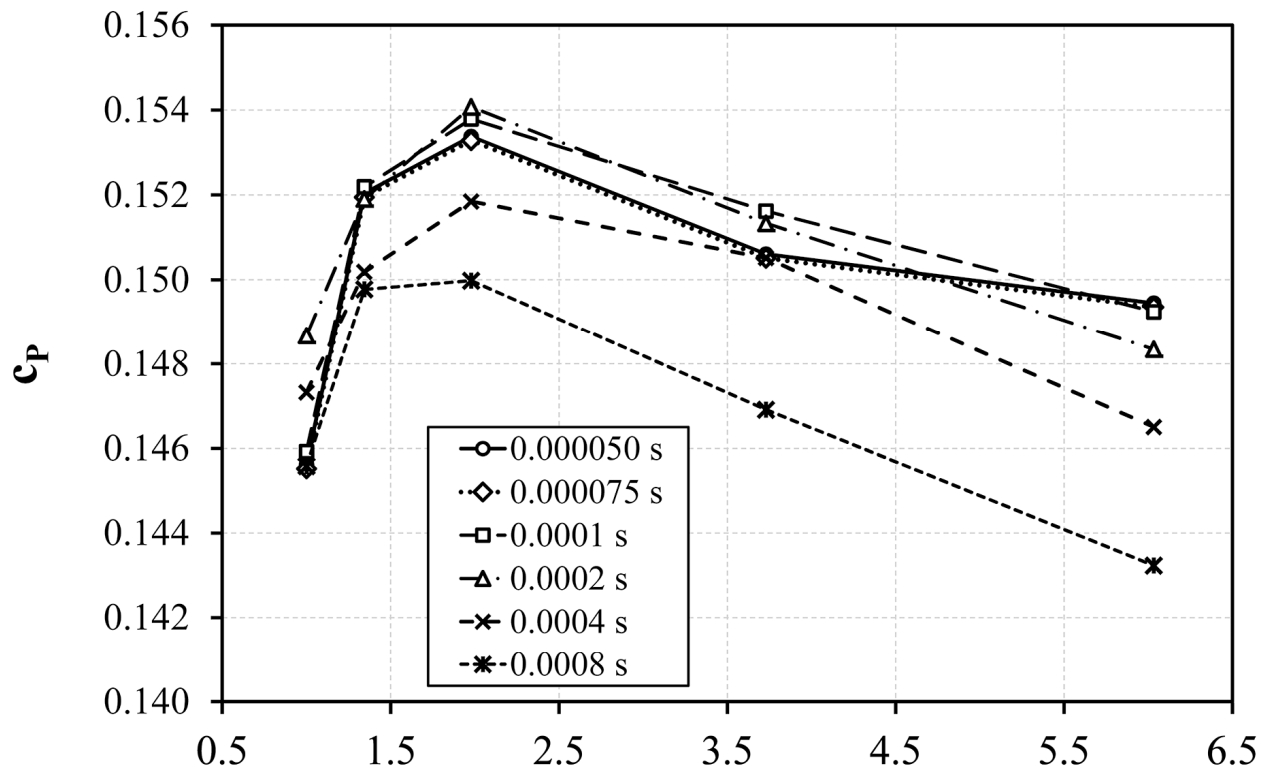


833

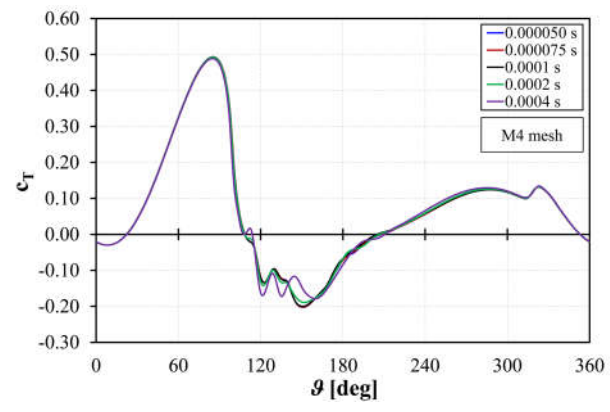


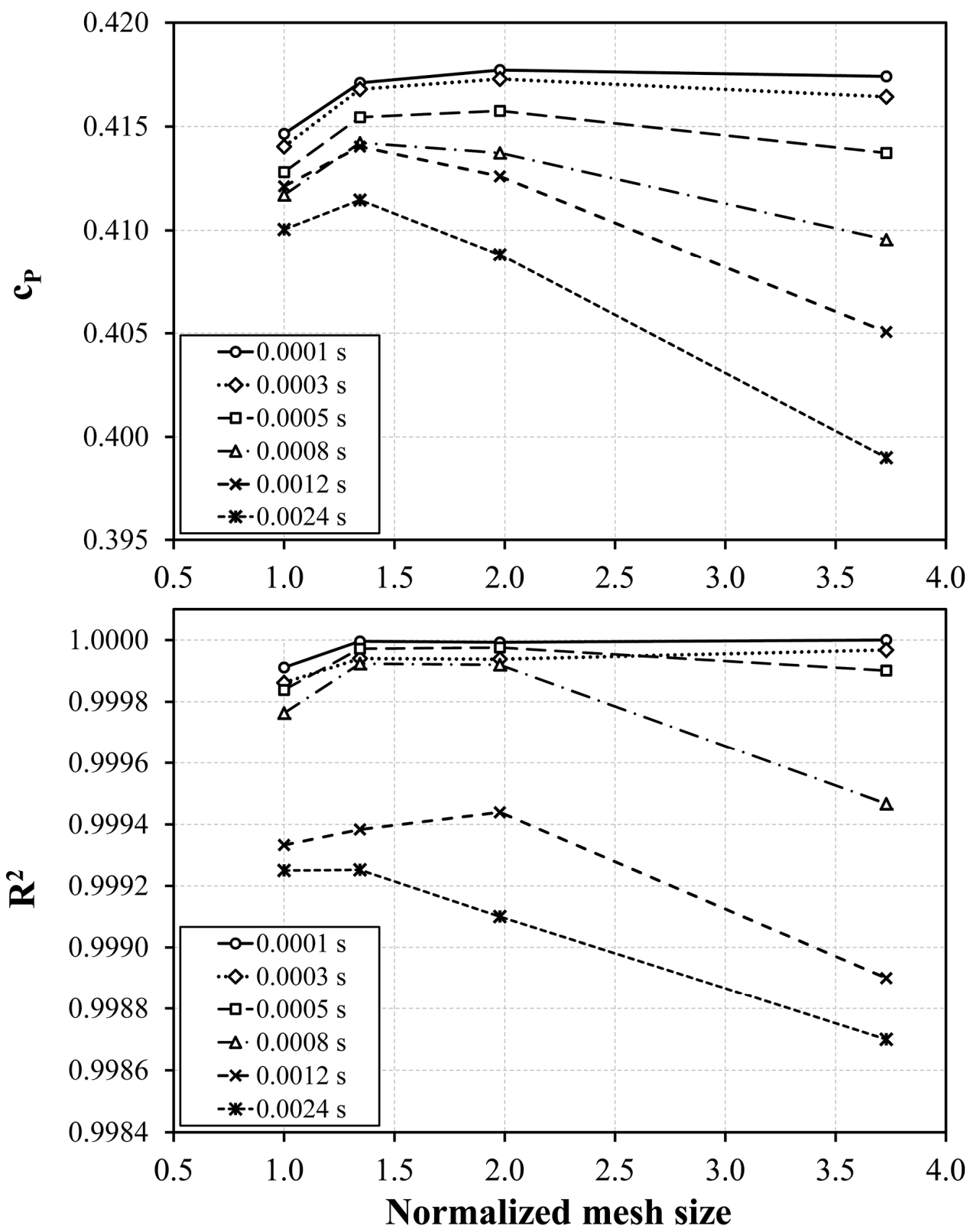
834

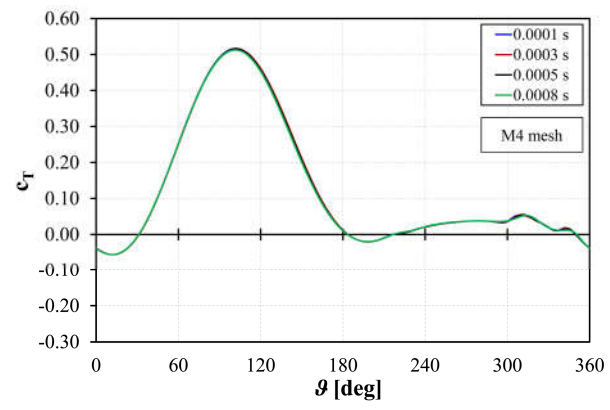


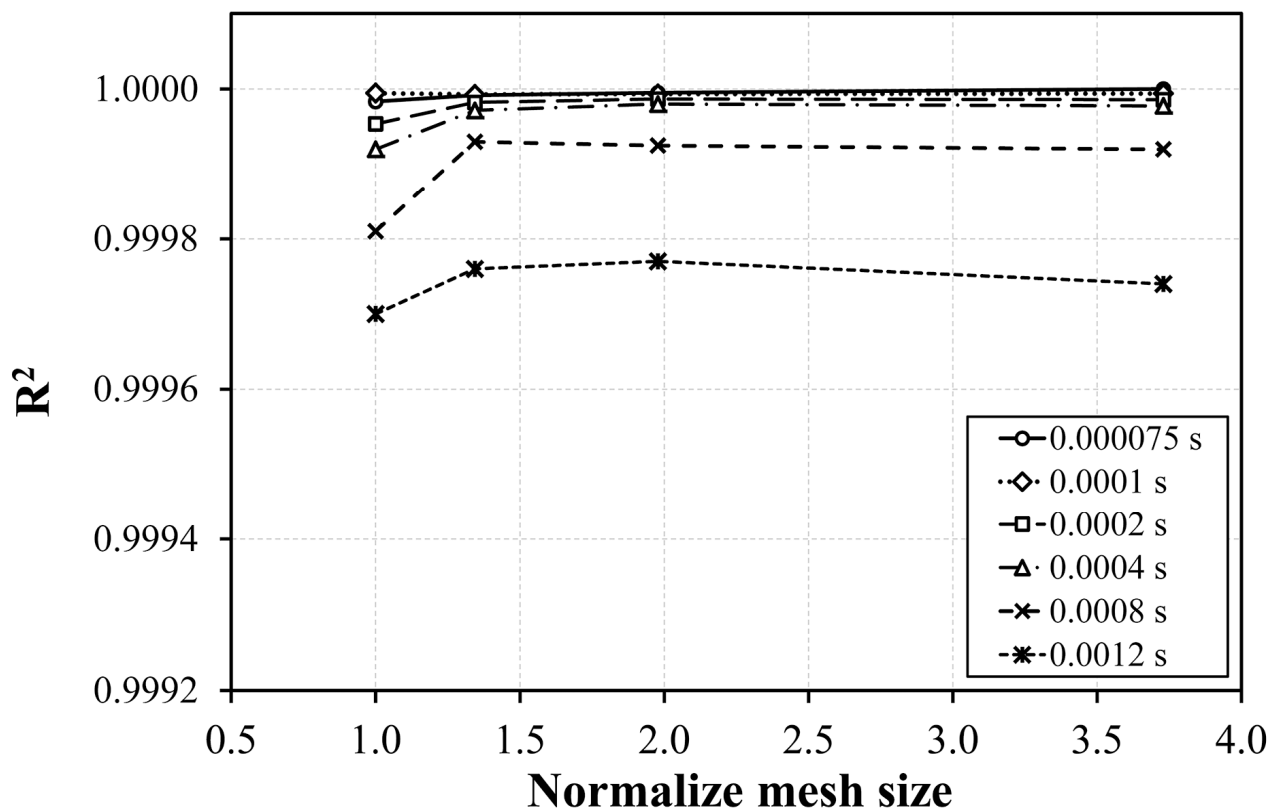
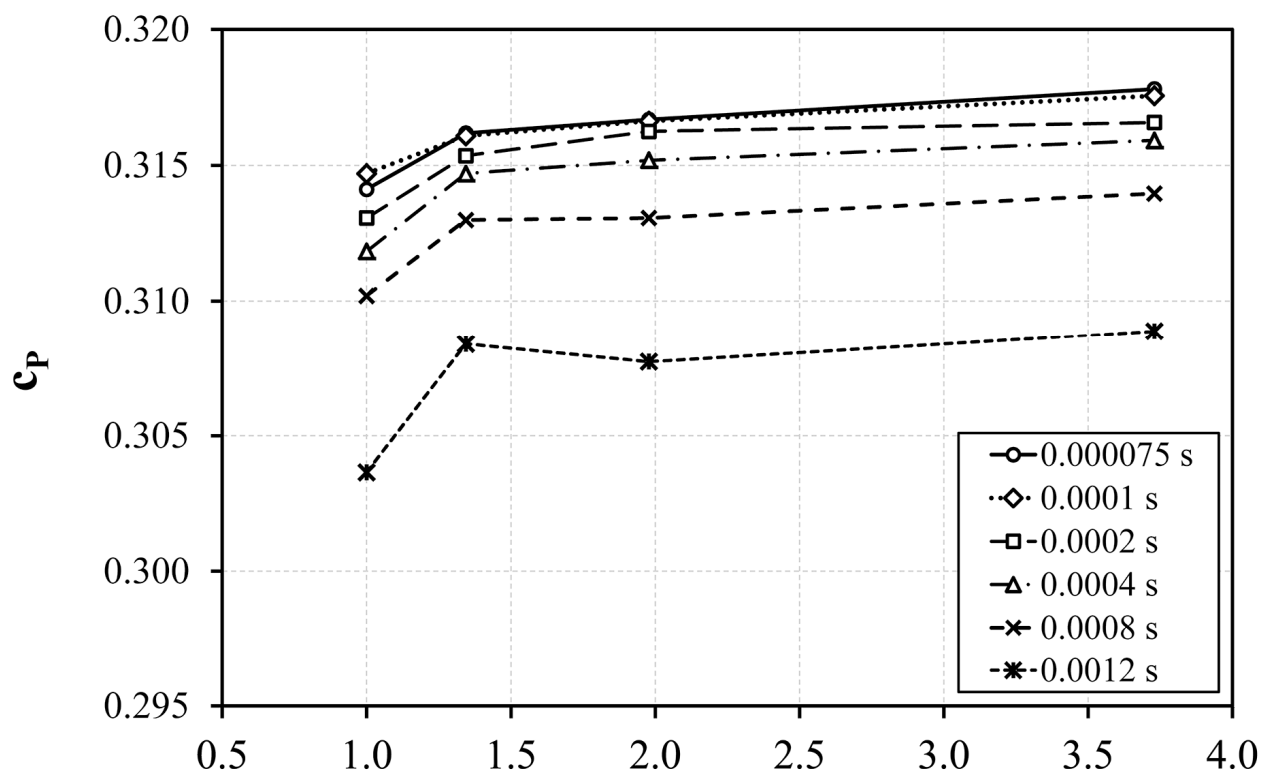




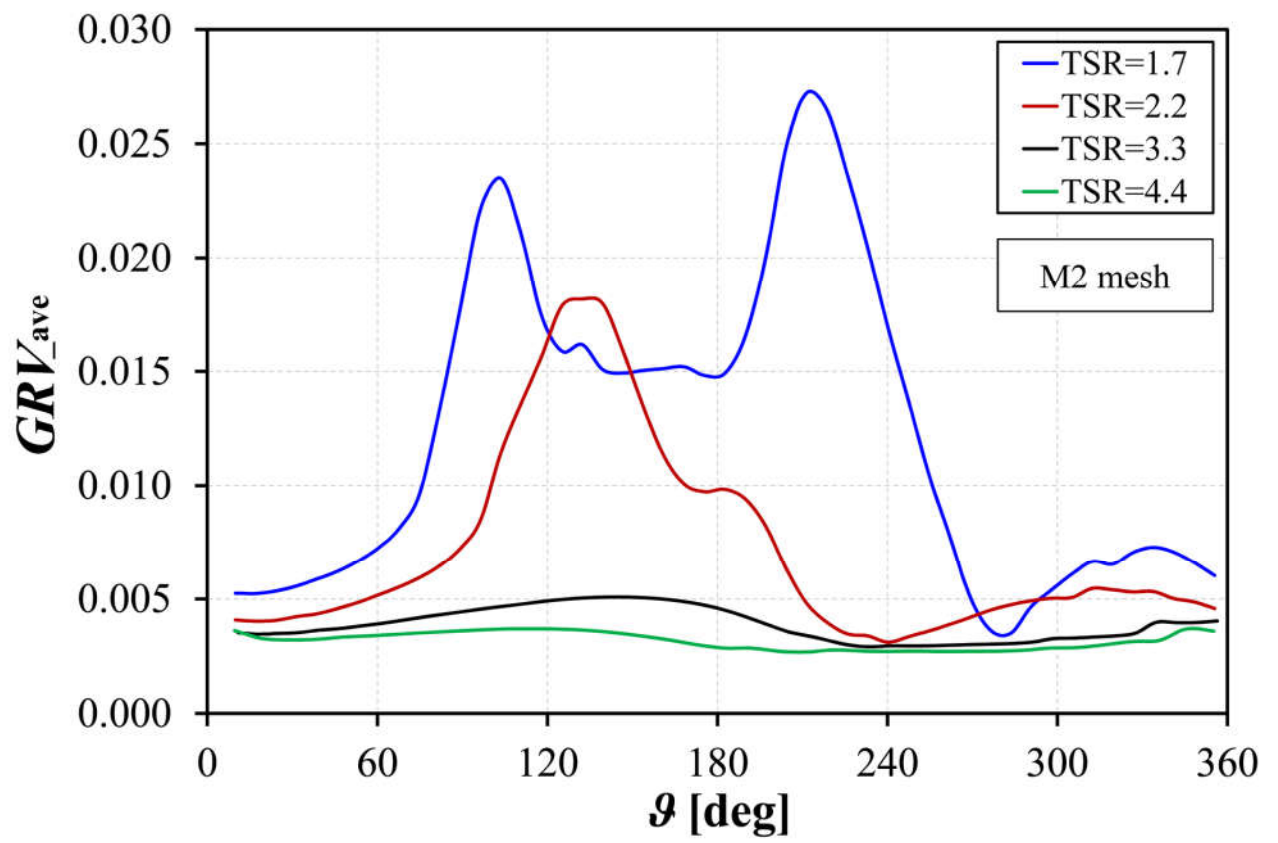
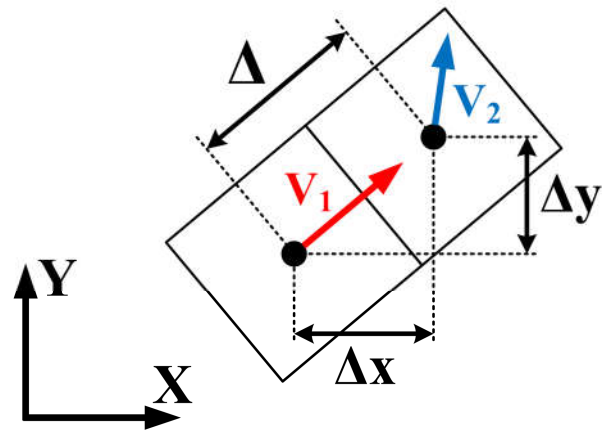




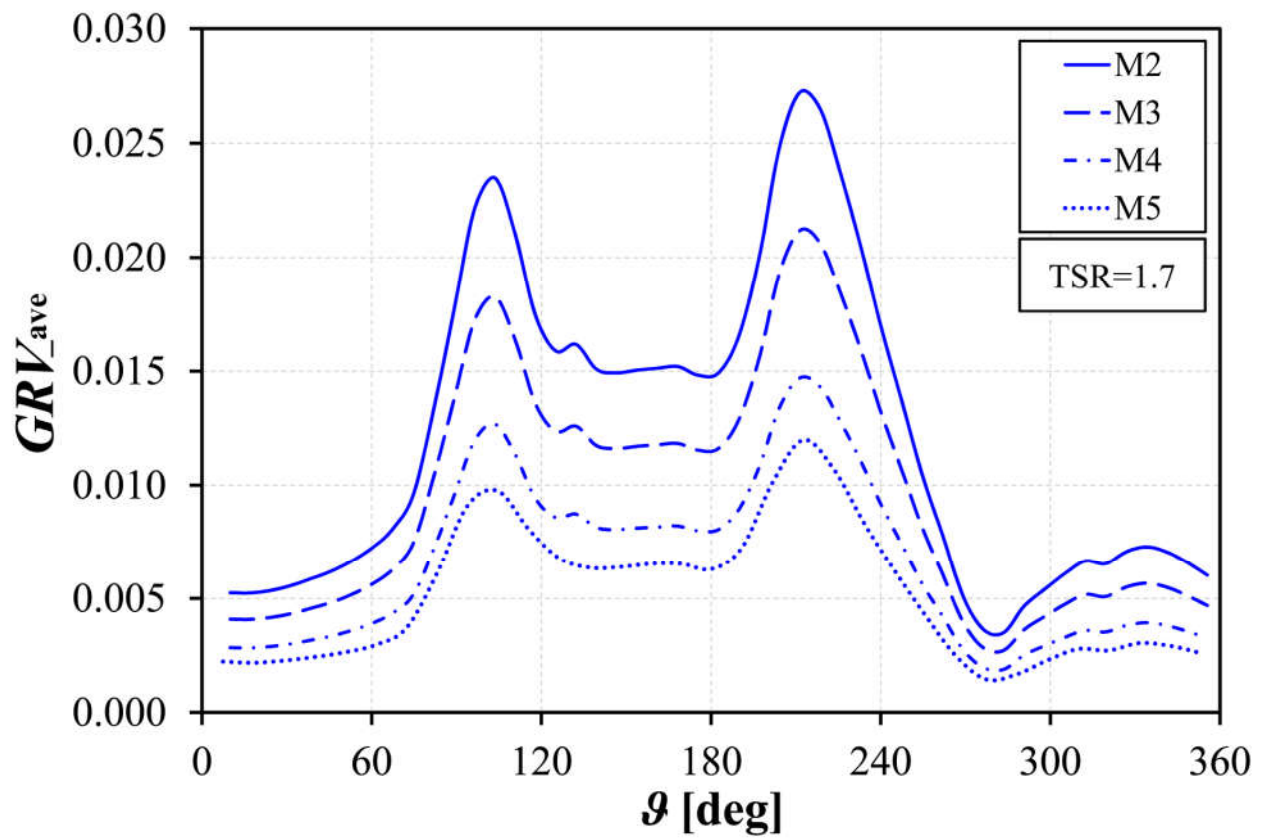




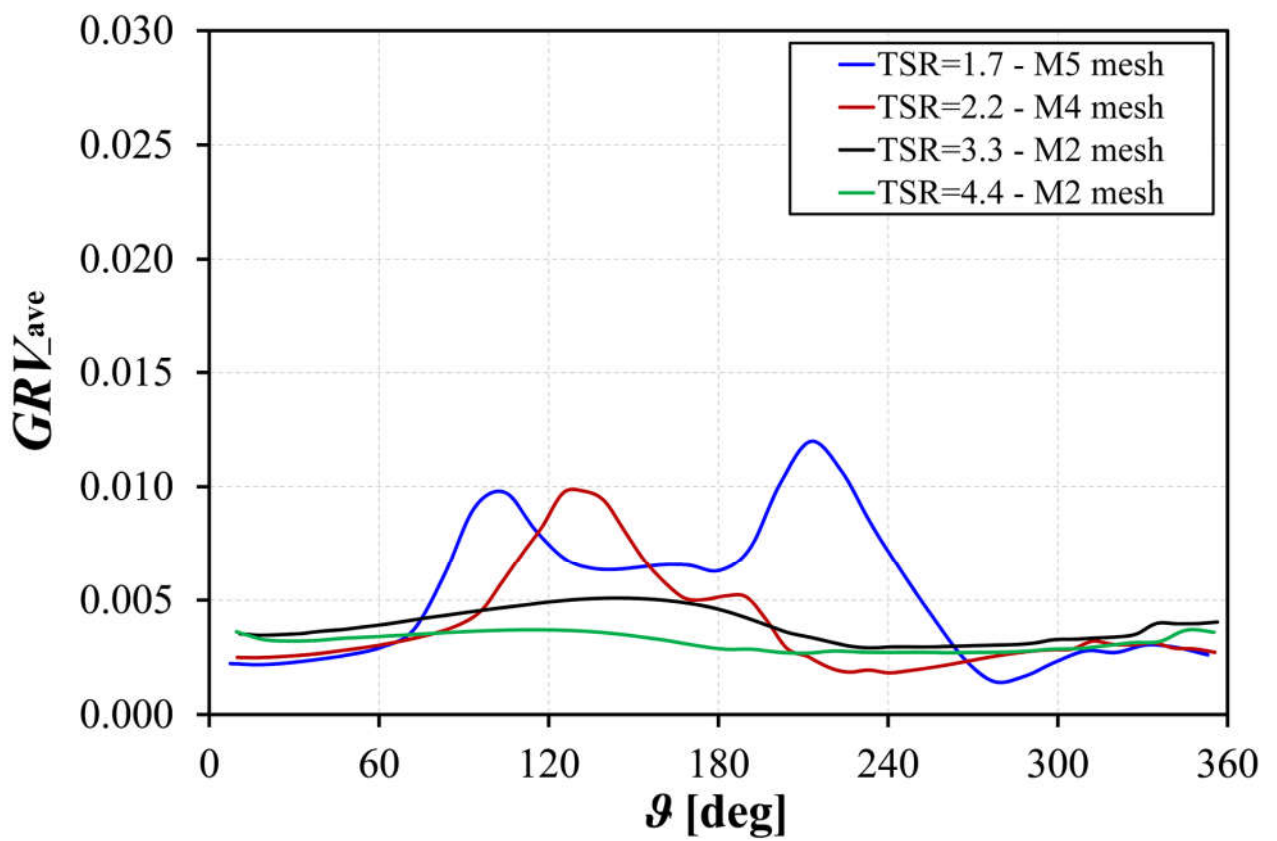
840



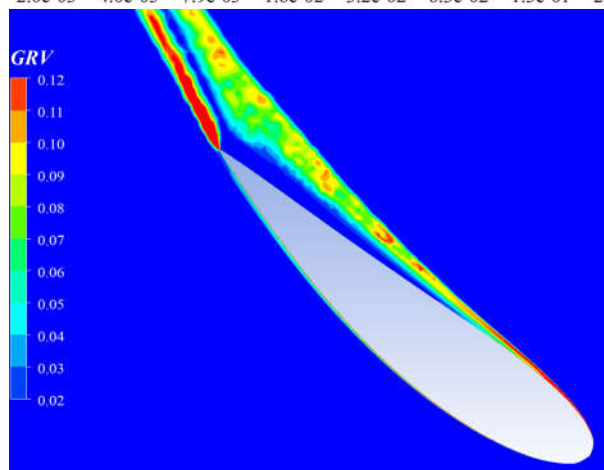
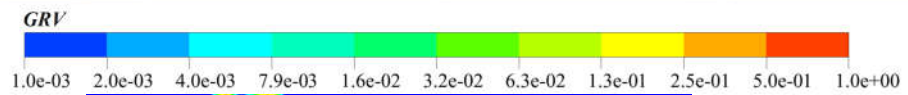
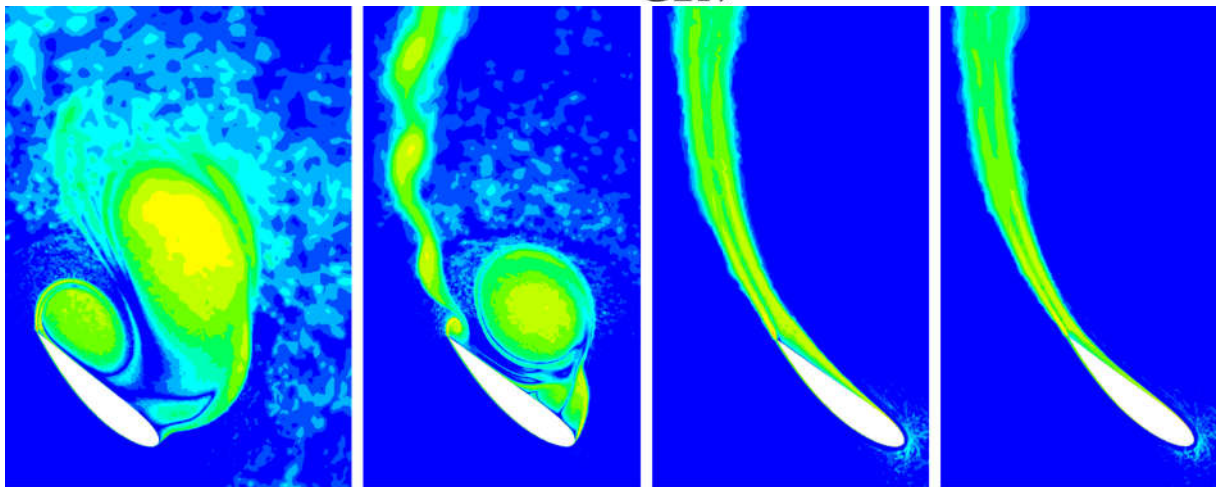
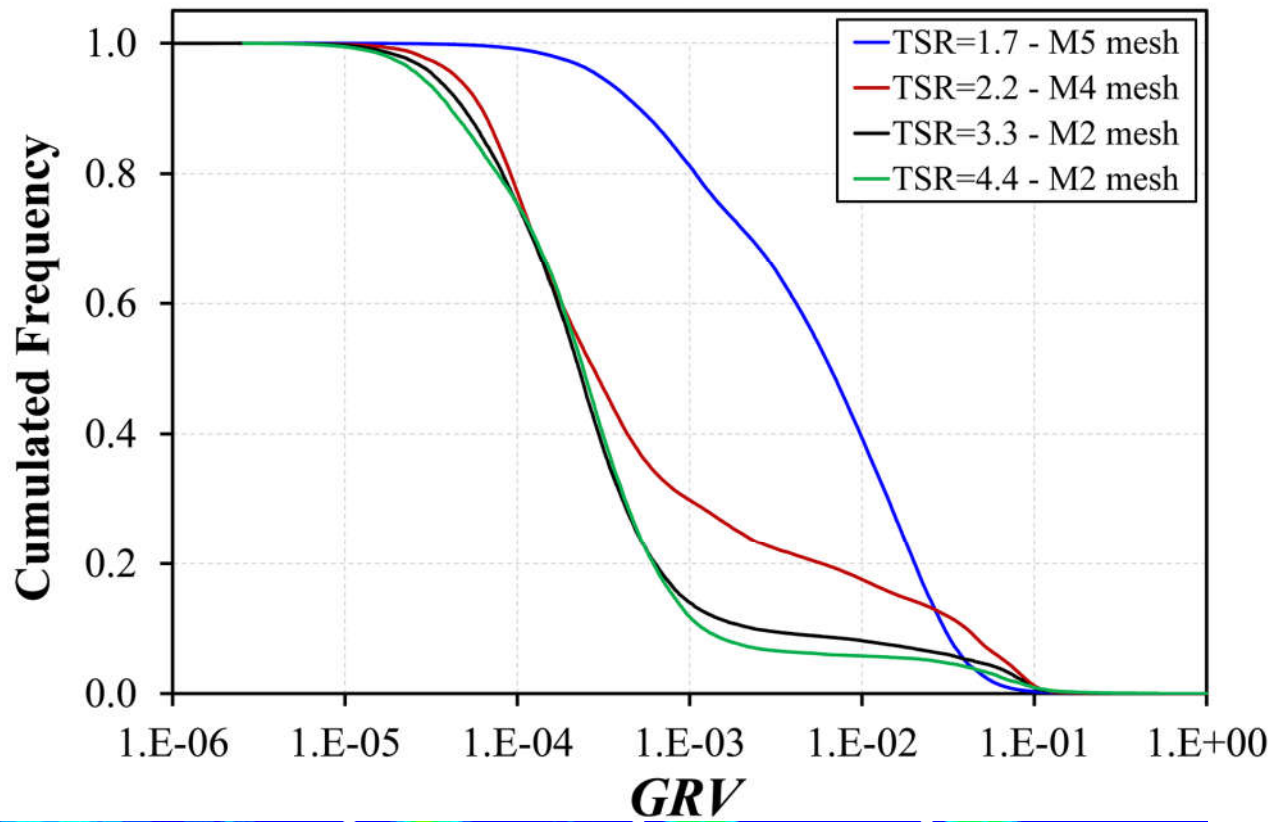
841

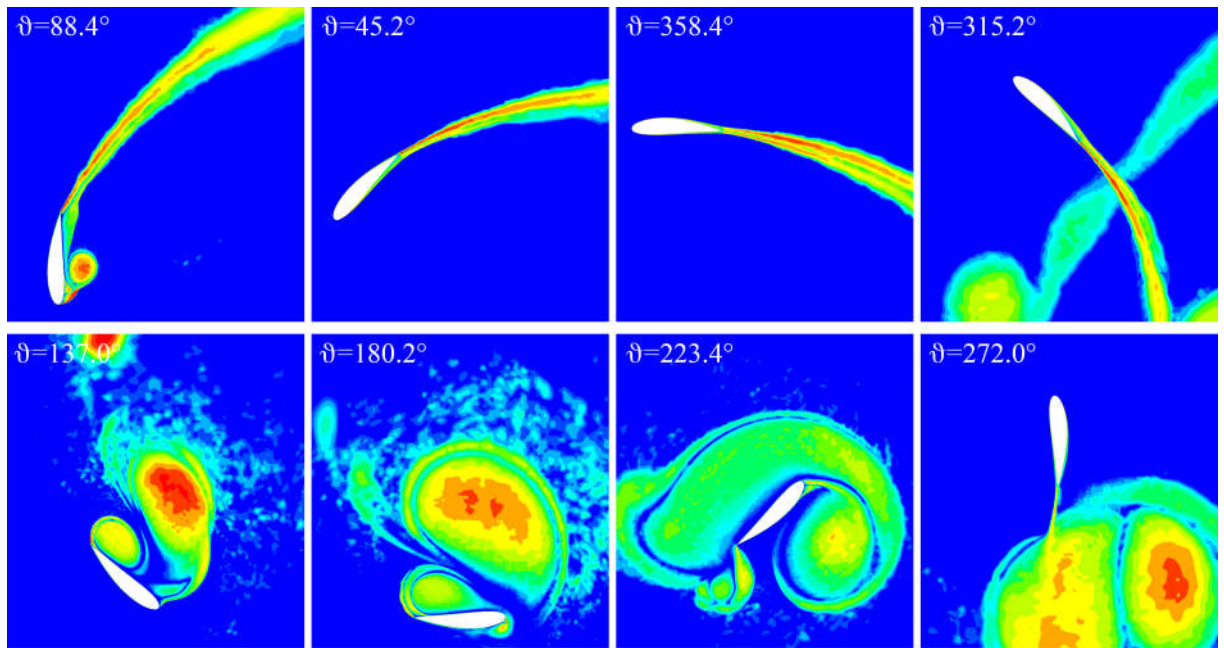


842

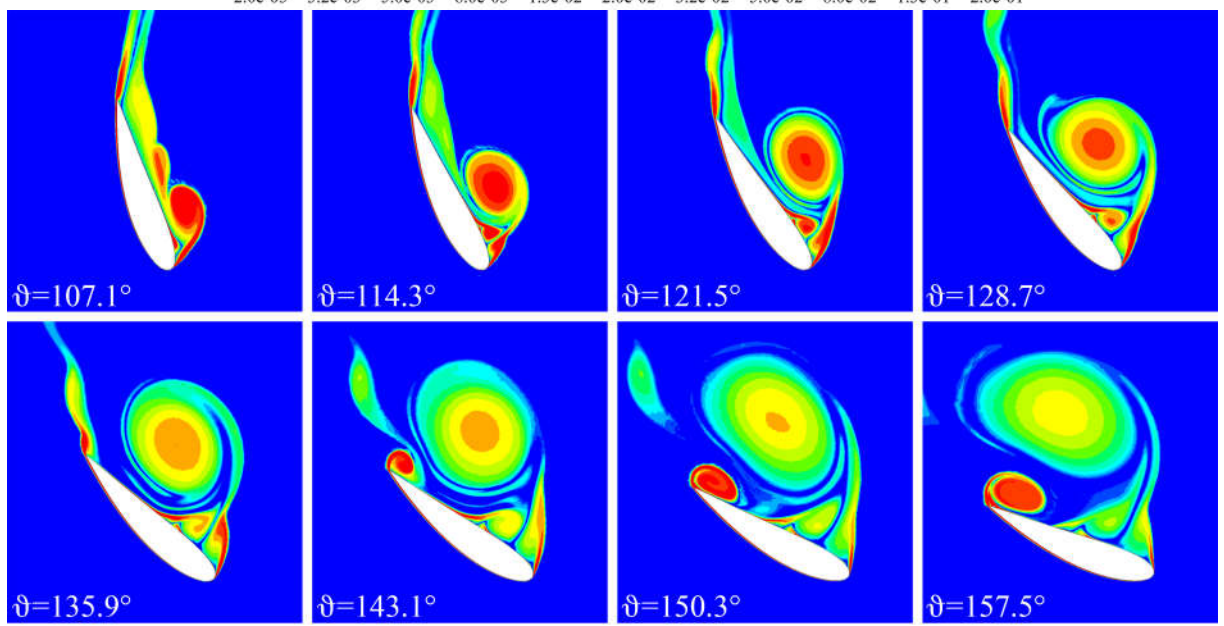


843





847



848